Investigating the effect of porous transport layer defects on structural and transport properties in proton-exchange-membrane water electrolyzers

Abdullah Tayyem, Victor Lefebvre, Junghyuk Ko, Sung Ki Cho, Jong Hyun Jang, and Jason Keonhag Lee

2026

Energy Conversion and Management 350 (2026) 120988

Contents lists available at ScienceDirect

Energy Conversion and Management

journal homepage: www.elsevier.com/locate/enconman

Investigating the effect of porous transport layer defects on structural and transport properties in proton-exchange-membrane water electrolyzers

Abdullah Tayyem [a,b], Victor Lefebvre [a,b], Junghyuk Ko [c], Sung Ki Cho [d], Jong Hyun Jang [d,e,f], Jason Keonhag Lee [a,b,*]

[a] Department of Mechanical Engineering, University of Victoria, Victoria, BC V8P 5C2, Canada
[b] Institute for Integrated Energy Systems (IESVic), University of Victoria, Victoria, BC V8P 5C2, Canada
[c] Division of Mechanical Engineering, Department of Mechanical Engineering, Korea Maritime and Ocean University, Busan 49112, the Republic of Korea
[d] Center for Hydrogen and Fuel Cells, Korea Institute of Science and Technology (KIST), Seoul 02792, the Republic of Korea
[e] Division of Energy & Environment Technology, KIST School, University of Science and Technology (UST), Seoul 02792, the Republic of Korea
[f] Graduate School of Energy and Environment, KU-KIST Green School, Korea University, Seoul 02841, the Republic of Korea

ARTICLE INFO

Keywords:
Water electrolysis
Porous transport layer
Defect
Pore network modelling
Stochastic modelling

ABSTRACT

Cost reduction of clean hydrogen is of utmost priority to leverage widespread adoption of hydrogen technologies, and porous transport layers (PTL) are known to be a significant cost driver for proton-exchange-membrane (PEM) water electrolyzers. This study reveals how the key morphological defects in the PTL that arise during manufacturing process can critically impact the performance of PEM water electrolyzers. A sintered titanium powder PTL was chosen as the baseline configuration for this model, due to its widespread use in commercial PEM water electrolyzers. Stochastic modelling is used to examine defects including thickness variations, positive protrusions, pinholes, porosity variations, cracks, and negative protrusions. Pore network modelling is used to characterize the impact of each defect on the transport properties, including single-phase and two-phase permeability as well as oxygen saturation profiles. Simulation results reveal that thickness variations and positive protrusions are defects that severely affect electrolysis, stemming from poor contact with the catalyst layer. They also significantly reduce single-phase permeability by increasing tortuosity. Furthermore, thickness variations and positive protrusions reduce water's effective permeability by causing flooding of oxygen gas, preventing reactant water from reaching reaction sites. In contrast, cracks, negative protrusions, and pinholes are defects with minor impact on electrolysis. In fact, they enhance the single-phase and two-phase permeability of liquid water in the through-plane direction. Finally, we suggest an effective remediation strategy for certain defects, which is to simply reorient the defect PTL during cell assembly to mitigate the negative impacts. Implementing these strategies will contribute in reduction of capital costs for PEM water electrolyzers.

1. Introduction

Concerns on climate change is becoming a serious issue as recent studies show that Earth has exceeded 1.5 °C of warming for the first time in 2025 compared to the preindustrial era [1]. This highlights the importance of developing decarbonization technologies to combat climate change. The industrial sector currently contributes up to 21% of global greenhouse gas emissions, with the production of chemicals, minerals, and metals responsible for nearly 93% of industrial CO_2 emissions [2]. Hydrogen is a promising avenue that can decarbonize industries such as steel and ammonia production [3]. However, this is built on a premise that hydrogen is produced with a low carbon footprint. 76% of the hydrogen produced today is derived from natural gas, via steam methane reforming, whereas water electrolysis contributes only 1–2% globally [4]. Deployment of proton exchange membrane (PEM) water electrolyzers at larger scale is necessary to shift from reforming of hydrocarbons to electrolysis [5]. PEM electrolyzers are particularly appealing due to their wide range of current densities, compact and stackable design, ability to operate dynamically with intermittent renewable energy sources, low operating temperature, and high pressure and volumetric flow rate production [6].

Catalyst layer (CL), PEM, and porous transport layer (PTL) are core

* Corresponding author at: Department of Mechanical Engineering, University of Victoria, Victoria, BC V8P 5C2, Canada.
E-mail address: jasonklee@uvic.ca (J.K. Lee).

https://doi.org/10.1016/j.enconman.2025.120988
Received 5 November 2025; Received in revised form 9 December 2025; Accepted 22 December 2025
Available online 27 December 2025

components in the PEM water electrolyzer [7]. Specifically, the titanium porous transport layer is particularly important because it is responsible for facilitating transport of reactant water and product oxygen gas, providing electrical conduction pathways, and supporting the mechanical stability of the membrane-electrode-assembly (MEA) [8]. Moreover, the PTL structure is known to have a dominant effect on interfacial contact and catalyst utilization, and therefore controlling its structure is mandatory to minimize undesired losses and reduce operating costs as the titanium PTL contributes up 25% of the total PEM electrolyzer cost [9,10].

Numerous studies have demonstrated the strong correlation between electrolyzer performance and PTL structural properties, including pore diameter distribution, porosity, tortuosity, surface roughness, thickness, single-phase permeability, and transport properties like effective and relative permeability [11–18]. However, the difficulty and high cost of processing titanium—which requires high temperatures and an inert atmosphere—restrict the development of new designs [11]. To implement novel PTL designs, Lee et al. have developed stochastic pore network modeling to evaluating transport and structural characteristics [12]. Previous studies primarily aimed to identify the optimal structural features of conventional PTLs, to improve mass transport and interfacial contact. Xu et al. [7] conducted a structural optimization study on the porous transport layer of sintered powder titanium PTL and calculated permeability using the lattice Boltzmann method. They recommended that the average pore size should be over 10 μm, and the porosity should be above 30%, since increasing pore size and porosity improve transport but decrease interfacial contact. Lee et al. [13] used pore network modeling to optimize the trade-off between permeability and interfacial contact of titanium PTL powder. They recommended a pore diameter of 25 μm and a porosity of 26.5% at non-starvation conditions, and the same pore diameter with a porosity of 40.5% at starvation conditions. Ito et al. [14] experimentally investigated felt PTL fiber sizes and porosities to determine the optimal pore configurations. They indicated that performance improved as pore size decreased for pores larger than the threshold size of 10 μm. Liu et al. [15] used X-ray computed tomography imaging and image binarization to reconstruct sintered powder PTL microstructures and used their lattice Boltzmann modeling to indicate that higher porosity and larger pore sizes enhance mass transport, while PTL with lower porosity and smaller pores offers better interfacial contact.

Other works have experimentally shown that innovative PTL structure enhances electrolyzer performance. Schuler et al. [16] modified the structure of titanium PTL to create a multilayer structure by utilizing different microporous layers (MPLs). Their research showed that MPLs improve contact with CL, leading to reduced mass transport losses and higher catalyst utilization. Mo et al. [17] adjusted the thickness parameter by creating a very thin titanium porous transport layer, measuring 25 μm thick, using nanomanufacturing technology. The PEM electrolyzer with this layer operated at a current density of 2.0 A/cm^2 and a voltage of 1.69 V. Yang et al. [18] developed a PTL titanium felt surface patterning method using laser processing and polytetrafluoroethylene hydrophobic treatment, reducing mass transport overpotential by 85.4% during high current density PEM operation. Lee et al. [19] developed custom PTLs with patterned through-pores, reducing the electrolyzer's mass transport overpotentials by up to 76.7%. Garkusha et al. [20] experimentally developed thin PTLs with micro-sized pinholes by using ultrashort laser pulses, achieving a porosity of 63%. While these pioneering studies experimentally demonstrate the importance of PTL structures, there is a lack of understanding on how defects in PTLs impacts water electrolyzer performance. Various types of defects may arise during manufacturing of porous materials, [21–23] and if it can be identified that certain defects are not as crucial to performance than the other, cost reduction could be substantial.

This study utilizes stochastic and pore network modeling to characterize six PTLs with different defects. The defects investigated include thickness variations, positive protrusions, pinholes, porosity variations, cracks, and negative protrusions. Our simulations will inform insights on how these defect types influence both transport and structural properties, and offer quality control strategies for manufacturing facilities to support in identifying which PTL defects could be used in the electrolyzer.

2. Methodology

A baseline sintered titanium PTL and six defect PTLs were generated computationally using a stochastic modeling approach. Only the underlying network statistics are generated stochastically (pore diameters and their x, y, and z coordinates), while the defect morphologies and size ranges are deliberately prescribed. Model validation of stochastic generation was conducted in previous studies. [12,13,24] Structural properties of each defect PTL were obtained via pore network extraction, and the two-phase transport was simulated using pore network modeling. Additionally, tortuosity was calculated as a property that influences single-phase transport and subsequently mass transport losses [25]. Moreover, surface roughness was evaluated as a metric to assess the contact between the PTL and the catalyst layer [13].

2.1. Stochastic modelling of the baseline PTL

All of the PTLs investigated in this work, including baseline PTLs and PTLs with defects, were generated using in-house stochastic models. Sintered titanium powder-based PTLs were selected as the baseline for this work due to their extensive use as standard anode PTLs in numerous experimental PEMWE studies, making them a reliable reference for modelling [26–28]. In addition, prior work on tape-cast and sintered Ti powder sheets has shown that manufacturing parameters strongly influence the porosity, pore size, and thickness of large-area PTLs. [29] These processing sensitivities make sintered titanium powder PTLs particularly well suited for a defect-focused study. Furthermore, sintered powder-based materials are widely used in the filtering industry, [30] and the defects examined have been selected from the most common ones. [21–23] Three base PTLs with identical structural properties including domain size, target porosity, powder radius, and sinter-necks were randomly generated to establish a baseline to be compared with the PTLs defects. Although defects were only added onto Base1, generating 3 bases allowed for the computation of mean values leading to a more reliable comparison result. The porosity profiles of the 3 baseline PTLs are as shown in Fig. S1 in the Supporting Information. The processes for generating baseline PTLs can be found in our previous works and is available in the Supporting Information. [31].

2.2. Defects implementation

Fig. 1a shows the baseline PTL generated, and parts Fig. 1b ~ g display schematics for all defect types investigated in this study, including thickness variations, positive protrusions, pinholes, porosity variations, cracks, and negative protrusions, respectively. These defects were selected based on defects commonly found in titanium alloy, [21] metal fiber sintered sheets [22], and titanium porous structures manufactured by electron beam and selective laser melting [23]. The first four defects were incorporated into the baseline PTL, base #1, using a combination of additions and subtractions of the defect feature. The location of positive and negative protrusions and pinholes was selected arbitrarily, with a single defect created in the baseline PTL. It is important to note that the location and quantity of defects can significantly influence the transport of both reactants and products. For example, Kim et al. [32] found via synchrotron X-ray imaging that a higher content of oxygen was observed with the use of PTL with through pores (pinholes that pass across the PTL thickness) under both the channels and the lands when compared to PTL with through pores only under the channels. Protrusions of precise radius were manually added to specific coordinates, creating a single powder protrusion onto the

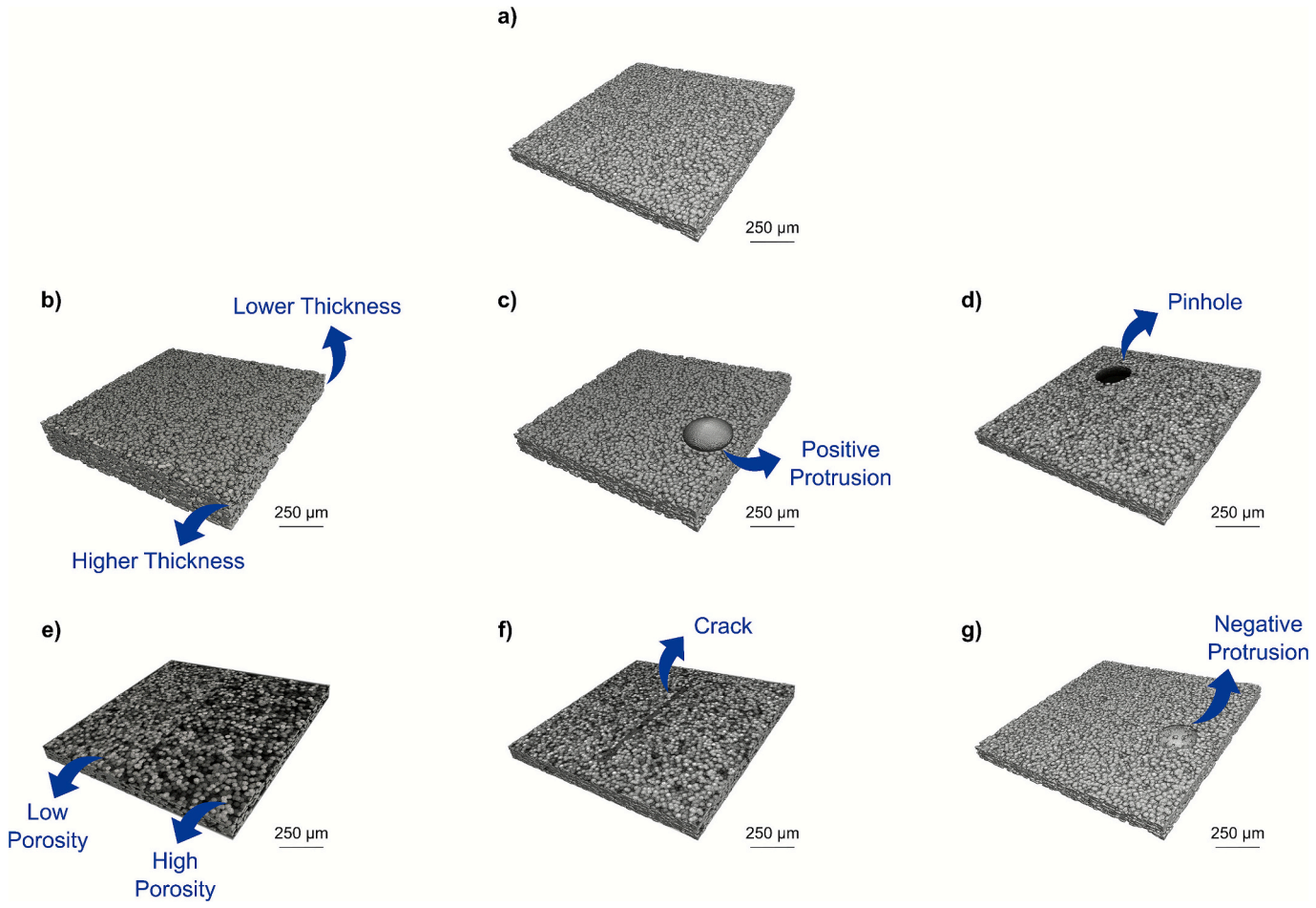

Fig. 1. Stochastically generated PTLs showing different cases: (a) baseline, (b) thickness variation defect, (c) positive protrusion defect, (d) porosity variation defect, (e) crack defect, and (f) pinhole defect.

baseline PTL. The reverse process was applied to generate the negative protrusion. The pinhole defect was created by precisely cutting a vertical cylinder through the entire thickness of the baseline PTL. Lastly, the cylindrical crack length was designed to be a surface crack at the center of the domain (500, 500) µm with a crack length of 800 µm covering 80% of the total PTL length (1000 µm) for all crack radius cases investigated. The cylinder was then subtracted to baseline PTL base #1, mimicking the crack defect. For the porosity variation, two PTL with different target porosity were stochastically generated, but the width of each was divided in half. Both PTLs were then fused side by side to create a single PTL with two different porosities. The last defect, thickness variation, was developed using only stochastic modelling. In order to create a different thickness, the domain of the randomly generated powder was simply modified to obtain a straight slope increasing thickness. Powder was also added to the thicker PTL to accommodate the larger volume while keeping a constant porosity. Therefore, the porosity profile of the thickness variation and porosity variation differs from the baseline PTL. Each defect was reproduced multiple times with some variation in size to better analyze the impact of each individual type of defect. A total of 17 PTLs with 6 distinct defect types were created with 20 total PTLs including the three baselines.

2.2.1. *Thickness variation defect*

Three different thickness variations were generated and simulated with variations of 20%, 40% and 60%. Since the original thickness was kept constant at 250 µm, the thickness of the thickness variations linearly increased accordingly to 300, 350 and 400 µm.

2.2.2. *Positive protrusion defect and pinhole defects*

Three different-sized protrusion defects were generated with radius of 25, 50, and 100 µm, respectively. Each was added to the same coordinates onto the surface of baseline PTL 1. This resulted in 3 defective PTLs of 38% porosity, enabling individual analysis of its impact on the performance of the PTL. Pinhole defects that pass across the full PTL thickness were also generated with three different radius sizes of 25, 50, and 100 µm. The centroid of the cylinder representing the pinhole is positioned in the identical location as the baseline PTL.

2.2.3. *Negative protrusion defect*

The same process was conducted for the negative protrusions as the positive protrusion. However, instead of addition a sphere of 25, 50, and 100 µm, it removed any of the titanium particle that was confined within the diameter of the protrusion, creating a massive pore at the surface of the defective PTL.

2.2.4. *Porosity variation defect*

Two different porosity variation defects were generated, from the baseline porosity of 38% to 60% and from 38% to 19%. This enables a comparison of the baseline porosity to a more porous structure and from the baseline porosity to a less porous structure.

2.2.5. *Crack defect*

Three crack defects were generated with radius sizes of 5, 10, 25 µm. Although in-house modelling enables the crack to be rotated in any angle parallel to the in-plane direction of the PTL, cracks in this study remained parallel to the in-plane axis. Position of the crack remained

identical throughout all three radius sizes.

2.3. Extraction of pore network

The Subnetwork of an Over-segmented Watershed (SNOW) algorithm developed by Gostick [33] is used for pore network extraction. The 3D coordinates, diameters, and volumes of pores and throats for each generated defect PTL were extracted from binary images to construct a pore and throat network for pore network modeling. Additionally, non-physical isolated pores were eliminated.

2.4. Pore network modelling

An open-source modelling package, OpenPNM [34], was used to conduct pore network modelling in this work. The two-phase flow is calculated using an invasion percolation algorithm to simulate drainage. Hydrophilicity and hydrophobicity are explicitly included via the contact angle: water is the wetting phase, oxygen is the non-wetting phase, and the oxygen–titanium contact angle is explicitly defined as 150° in the model. The basis of two-phase transport using pore network modelling has been explained in our previous work [35]. The effect of electrochemical reactions on gas production is represented through three oxygen inlet-coverage levels (10%, 50%, and 95%), representing low, medium, and high current density operation. A 95% oxygen coverage was chosen to realistically depict an operating condition where the CL/PTL interface is nearly flooded with oxygen gas at high current densities.

The following assumptions were used in the model: 1) The pores occupied with specific species is considered closed, in calculation of permeability of the other species. 2) Viscous forces are neglected and it is assumed that capillary forces control the quasi-static flow, where each pore can be filled with either water or gas, but not both simultaneously [36]. 3) All pores are initially filled with liquid water. 4) No phase change occurs, and the process is isothermal at a typical PEM operating temperature of 80 °C [37]. 5) No additional invasion occurs following the breakthrough of the gas phase. These assumptions were based from the previous literature, including studies by Altaf [36], Vorhauer [38], and Lee. [6] Table 1 lists all constant parameters used in the model.

It is important to note that this work does not predict the dynamic behavior of bubbles; instead, it simulates pore-to-pore invasion of quasi-static flow to model drainage. The percolation process has also been demonstrated by Arbabi et al., [40] where they used a microfluidic chip built from characteristics of a commercial PTL to visualize similarities with the invasion patterns from the model. The gas saturation profiles from the simulated model are also very similar to those obtained from operando imaging techniques results found by Lee at al. [41].

Absolute permeability, two-phase permeability, and relative permeability was calculated for both oxygen and water at various inlet oxygen coverages. Single-phase permeability measures how well liquid water transports to reaction sites in absence of a gas phase, whereas effective permeability of water describes its ability to transport when gas-filled pores are also involved (gas-filled pores are treated as closed pores) [13]. The permeabilities were determined by solving Stokes' equation and Darcy's law. Initially, the net flow into each pore was calculated using the mass conservation principle for individual pores:

Table 1
Physical properties incorporated in the model.

Parameter	Value	Reference
Water contact angle	150°	[37]
Operation temperature	80°C	[37]
Surface tension of water	0.0728 $N.m^{-1}$	[37]
Oxygen molecular weight	32 g/mol	[39]
Oxygen viscosity	2.3479e-5 Pa·s	[39]
Oxygen molar density	34.531 mol/m^3	[39]

$$q_i = \sum_{j=1}^{n} g_{h,ij}(P_j - P_i) = 0 \quad (1)$$

where q_i is the net flow into pore i ($m^3 \cdot s^{-1}$), P is the pressure at each pore i and j (Pa), and i and j represent neighboring pores. The Hagen-Poiseuille model was used to find the hydraulic conductivity $g_{h,ij}$ ($m^4 \cdot s \cdot kg^{-1}$) for the cylindrical throat. [42]

$$g_h = \frac{\pi d^4}{128 L_t \mu} \quad (2)$$

In this context, μ represents the fluid's dynamic viscosity measured in $kg \cdot m^{-1}.s^{-1}$, L_t is the length of the cylindrical throat in meters, and d stands for the pore diameter in meters. The resistor law [13] is used to determine the overall conductivity of the pore throat and pore geometry:

$$\frac{1}{g_{h,ij}} = \frac{1}{g_{h,pi}} + \frac{1}{g_{h,t}} + \frac{1}{g_{h,pj}} \quad (3)$$

The total flow rate Q (m3/s) was found by solving Equation (1) as a system of linear equations with boundary pressures specified at the inlet and outlet surfaces, where p refers to pores and t indicates the throats. Finally, Darcy's law [43] was used to calculate permeability:

$$K = \frac{Q.\mu.l}{A(P_1 - P_2)} \quad (4)$$

where K represents permeability (m^2), A is the in-plane area (m^2), P_1 and P_2 are the boundary pressures, and l is the length of the network in the through-plane direction (m). After running the invasion percolation algorithm, the effective permeability of both phases in the defect PTLs was calculated in all directions. At this stage, because invaded pores by gas can no longer be accessed by water, it is assumed that these pores no longer contribute to hydraulic conductance. [6] After adjusting hydraulic conductance based on pore occupancy, Darcy's law can be used again to calculate the effective and relative permeabilities of both phases in all directions. In this work, permeabilities are used as an indicator to describe the PTL's ability to transport liquid water and oxygen gas, and hence its mass transport abilities.

2.5. Surface roughness

The average roughness and root mean square roughness are used to assess the quality of the interfacial contact between the catalyst layer and the PTL. The average roughness [13] (S_a) is calculated by determining the mean height of each pixel in the image:

$$S_a = \left(\frac{1}{MN}\right) \sum_{i=1}^{M} \sum_{j=1}^{N} |Z_{ij}| \quad (5)$$

where M and N are the dimensions of the defect PTL in the domain, with i and j representing each pixel. Zij is the surface height of the material at position i and j. The root mean square roughness (S_q) was determined by averaging the root mean square roughness of the defect surface:

$$S_q = \sqrt{\left(\frac{1}{MN}\right) \sum_{i=1}^{M} \sum_{i=1}^{N} Z_{ij}^2} \quad (6)$$

2.6. Tortuosity

Tortuosity, τ (−), is another important metric used to assess fluid transport efficiency in porous media. It indicates the ratio of the actual flow path (L_a) to the thickness of the domain (L):

$$\tau = \frac{L_a}{L} \quad (7)$$

Tortuosity can also be determined with this formula: [31]

$$\tau = \frac{D}{D_e \varepsilon} \tag{8}$$

where D represents the intrinsic diffusion coefficient ($m^2 \cdot s^{-1}$), D_e stands for the effective diffusion coefficient ($m^2 \cdot s^{-1}$), and ε indicates the porosity (−). This work employs the open-source Python package TauFactor [44] to compute the tortuosity of the stochastically generated defect PTLs.

3. Results

3.1. Impact of defects on structural properties

Structural properties investigated in this study for different PTLs with different defect sizes include pore size distribution, porosity profiles across thickness, tortuosity, and surface roughness. Analyzing the impact of defects on structural parameters is essential because they

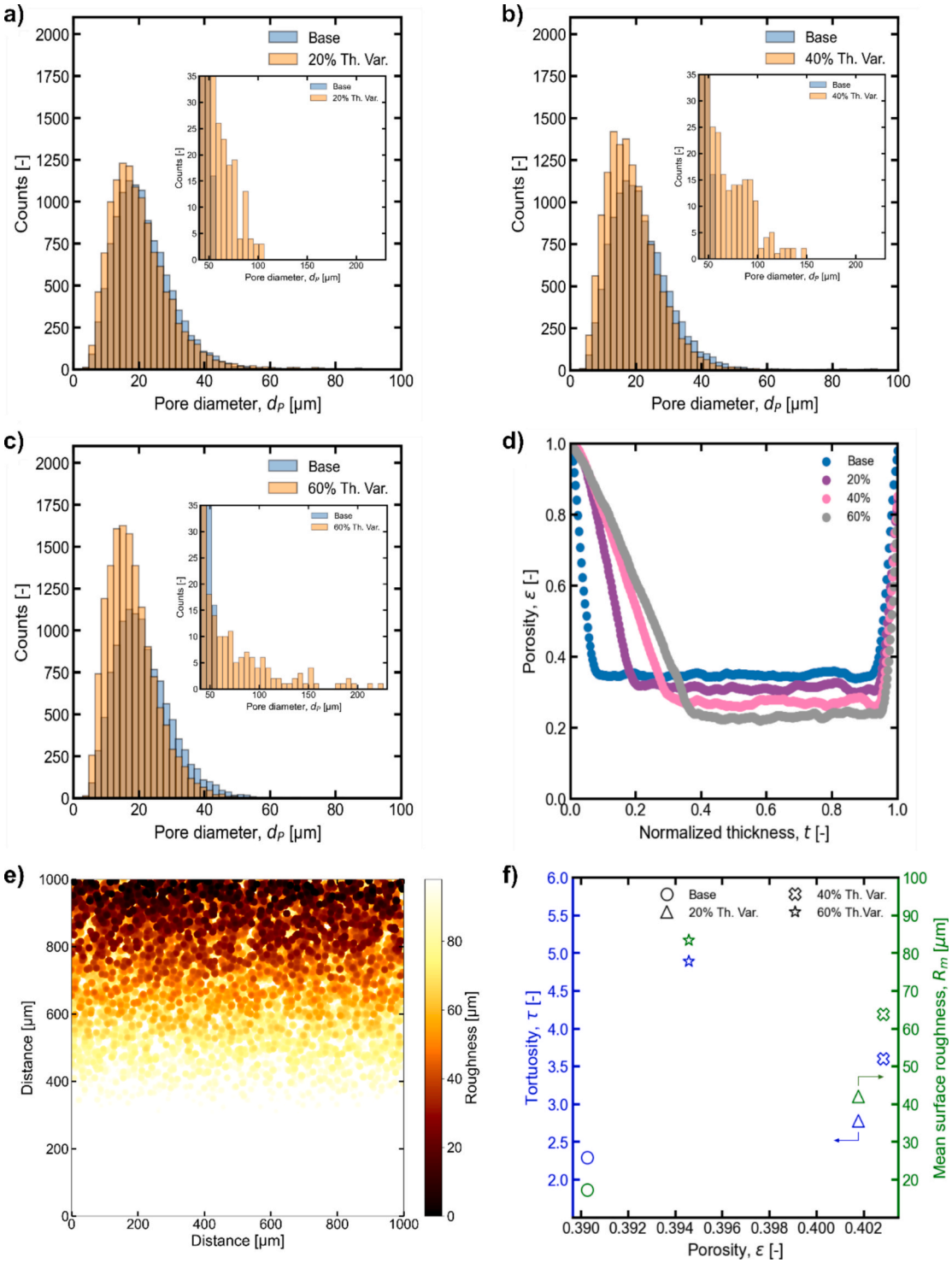

Fig. 2. Pore size distribution for defect PTLs with (a) 20%, (b) 40%, and c) 60% thickness variations. (d) porosity profiles for defective PTLs with the same thickness variation cases. (e) surface roughness map for defective PTL with 60% thickness variation. (f) porosity versus tortuosity and surface roughness for defect PTLs with the same thickness variation cases.

directly influence transport properties, which subsequently affect mass transport losses. Additionally, analyzing how defects affect surface roughness is as critical because it relates to the catalyst utilization. [45].

3.1.1. Thickness variation

Results show the formation of new pores within the overall structure of the defect PTL as additional titanium particles were added to create a sloped surface. Fig. 2a ~ 2c shows the pore size distribution for defective PTLs with 20%, 40%, and 60% thickness variations, respectively. The added structure includes the formation of new pores that are small (<20 μm) and large (>50 μm), with an increasing number of both pore types as the variation percentage rises. Inset figures show the number of large pores formed in each case. In the 20%, 40%, and 60% cases, the large pore sizes reach up to approximately 100 μm, 150 μm, and 250 μm, respectively. The increase in large pore sizes occurs due to the void space formed between the PTL and catalyst layer, which will behave as a delamination that would cause flooding. In contrast, the rise in smaller pore sizes occurs because of the newly added material from added

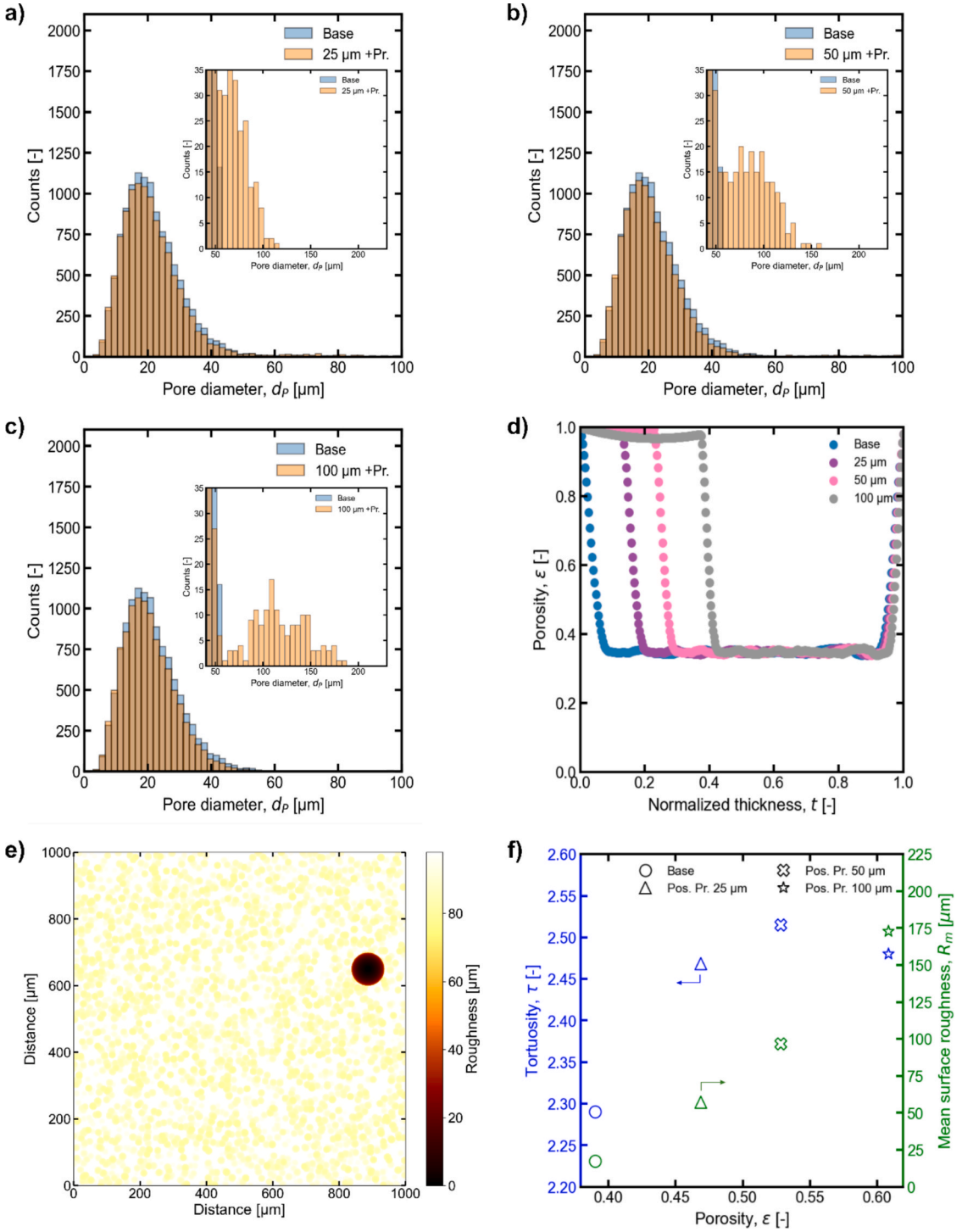

Fig. 3. Pore size distribution for defect PTLs with (a) 25 μm, (b) 50 μm, and (c) 100 μm positive protrusions. (d) porosity profiles for defect PTLs with the same positive protrusion cases. (e) surface roughness map for defect PTLs with 50 μm positive protrusion. (f) porosity versus tortuosity, and surface roughness in defect PTLs with the same positive protrusion sizes.

thickness. Basically, the newly added titanium particles in the thickness variation further adds the smaller pores. Moreover, it is important to note that porosity of the base section of the PTL (i.e. non-defect region) is lower with steeper thickness variation (Fig. 2d), contributing to increased number of smaller pores. Investigating deviations in pore sizes is crucial for the defect PTL, as pore size plays a significant role not only in single-phase but also two-phase and relative permeabilities [6].

The surface roughness map for the 60% thickness variation case is shown in Fig. 2e. Additionally, maps for the 20% and 40% cases are in Fig. S2 in the Supporting Information. It could be speculated that the interfacial contact between the defect PTL and the CL will be poor because of the thickness variation defect. Specifically, roughly 20% of the PTL will be in direct contact with the CL, while remaining defective regions would become sources of delamination. These regions of delamination will reduce electrical conductivity of the catalyst layer, subsequently decreasing catalyst utilization. [16] The larger the variation percentage, the greater the deviation from the average height and roughness values. Average surface roughness and tortuosity values were quantified in Fig. 2f. Surface roughness increased significantly from a baseline of 17.25 μm to 42.00 μm, 63.78 μm, and 83.41 μm at 20%, 40%, and 60% variation levels, respectively. Regarding tortuosity, cases with thickness variation showed the most significant increase among all the defects studied, rising from 2.29 at the baseline to 2.27, 3.60, and 4.89 at 20%, 40%, and 60% variation levels, respectively. Tortuosity values increased because thickness variation defects added more material to the PTL, creating more convoluted paths. The increase in tortuosity values indicates that defective PTL with thickness variation will experience higher mass transport losses. [46].

3.1.2. Positive protrusion

The impact of 25 μm, 50 μm, and 100 μm positive protrusions on pore size distribution is shown in Fig. 3a ~ 3c, respectively. No significant change is observed in the overall pore size distribution within the PTL for all cases because a positive protrusion is a local bulge created at the top of the original baseline PTL. However, the titanium protrusion leads to a layer of void space at the CL/PTL interface, and this void space will be considered as a layer of delamination. Therefore, positive protrusions create additional larger pores (>50 μm), as shown in the inset of Fig. 3a ~ 3c. Positive protrusions lead to pore formation with sizes up to 120 μm, 160 μm, and 180 μm for protrusions of 25 μm, 50 μm, and 100 μm, respectively. This impact can be seen from the porosity profile as well, (Fig. 3d). The porosity curve shifts right with introduction of protrusion, indicating that it is in fact causing delamination.

Fig. 3e shows the surface roughness map for the 50 μm positive protrusion case. Additionally, the roughness maps for 25 μm and 100 μm are included in the Supporting Information in Fig. S3. The localized height difference is clearly visible at the protrusion site for all protrusion cases. As titanium is rigid, it will not compress as carbon gas diffusion layers do. Hence, positive protrusion will undesirably harm the interfacial contact with the CL/PTL interface. Fig. 3f shows the average surface roughness and tortuosity values for the positive protrusion cases. After quantifying values, it was found that the most significant deterioration in roughness among all studied defects occurs in the positive protrusion cases. Roughness values increase approximately linearly from a baseline of 17.23 μm to 57.16 μm, 96.64 μm, and 172.82 μm for protrusion sizes of 25 μm, 50 μm, and 100 μm, respectively. Regarding tortuosity results shown in Fig. 3f, the tortuosity slightly increases when the protrusion defect is introduced, likely due to added thickness. However, the change in tortuosity values remains less than 4% with increasing size of the protrusion.

3.1.3. Pinholes

Pinholes have a minor impact on the overall pore size distribution and porosity profiles shown in Fig. S4 in the Supporting Information. Although a few large pores (>50 μm) are visible in the inset of the pore size distribution figures, their straight alignment creates a conduit through the PTL thickness that will reduce mass transport losses of PEM electrolyzers. [19].

Fig. 4a shows the surface roughness map for defect PTLs with a 50 μm pinhole. Additionally, the maps for 25 μm and 100 μm are included in Fig. S5 in the Supporting Information. The local increase in roughness is clearly visible at the pinhole site, where material is completely removed to create a conduit. Fig. 4b shows the quantified mean surface roughness values for defect PTLs with pinholes. Results show that the average surface roughness increased from 17.23 μm at the baseline to 17.76 μm, 19.21 μm, and 25.15 μm for sizes of 25 μm, 50 μm, and 100 μm, respectively. Roughness values gradually and nearly linearly increase with pinhole size because larger pinholes remove more material. This leads to bigger gaps at the PTL surface with very deep heights that extend across the PTL. However, the rise in the average roughness values in pinhole cases is considered reasonable when compared to other defect types like positive protrusions and thickness variations. This is because pinholes only increase roughness in a small local area, while thickness variations and positive protrusions raise roughness values across the entire surface.

Tortuosity values shown in Fig. 4b decrease almost linearly with pinhole size. The values drop from 2.29 at the baseline to 2.27, 2.22, and 2.07 for pinhole sizes of 25 μm, 50 μm, and 100 μm, respectively. Removing more material with larger pinhole sizes decreases the number of complex paths for the phase to pass through. Therefore, defect PTLs with pinholes will have lower tortuosity, thereby reducing mass transport losses. [46].

3.1.4. Porosity variation

In porosity variation cases, one side of the PTL has smaller pore sizes and lower porosity, while the other side has larger pore sizes and higher porosity. Fig. 5a ~ 5b show pore size distributions for 38%-19% and 38%-60%, respectively. As porosity decreases from 38% to 19%, the frequency of smaller pores with diameter less than 20 μm increases, while the frequency of larger pores with diameter greater than 50 μm decreases. Conversely, increasing porosity from 38% to 60% raises the number of larger pores and lowers the count of smaller pores. The porosity variation defect significantly affects pore size distribution because porosity is directly related to pore size. Examining the porosity profile in Fig. 5c will confirm this result, where the bulk porosity decreases in the 38%-19% case and increases in the 38%-60% case.

Fig. 5d shows the quantitative values of mean surface roughness. As porosity varies from 38% to 60%, the mean surface roughness increases from the baseline value of 17.23 μm to 24.03 μm because of larger pore sizes located at the PTL surface. Conversely, roughness decreases to 13.23 μm when porosity varies from 38% to 19% because roughness decreases as pore sizes located at the PTL surface become smaller. Contact between CL and PTL will be improved by decreasing pore size and porosity, while interface contact will be reduced by increasing pore size and porosity. [7] This result can also be confirmed by the surface roughness map for the defective PTL with 38%-19% porosity variation shown in Fig. 5e. The map shows brighter color on the 38% porosity side with higher roughness, and a darker color on the 19% porosity side with lower roughness. Additionally, the surface roughness map for the 38%-60% porosity variation case is included in the Supporting Information in Fig. S6. Consequently, PTLs with 38% to 19% porosity variation will have improved contact with CL, while PTLs with 38% to 60% porosity variation will have worse contact compared to baseline.

Tortuosity values were also quantified in Fig. 5d. Tortuosity increased from a baseline of 2.29 to 3.10 as porosity decreased from 38% to 19%. In contrast, tortuosity decreased to 1.67 as porosity increased from 38% to 60%. Tortuosity decreases with increasing porosity due to the formation of more void space, which makes the flow paths less convoluted. Increasing porosity and pore size will enhance transport efficiency by reducing tortuosity, and vice versa. [7] As a result, defective PTL with 38%-60% will have lower mass transport losses, and the 38%-19% case will have higher mass transport losses compared to

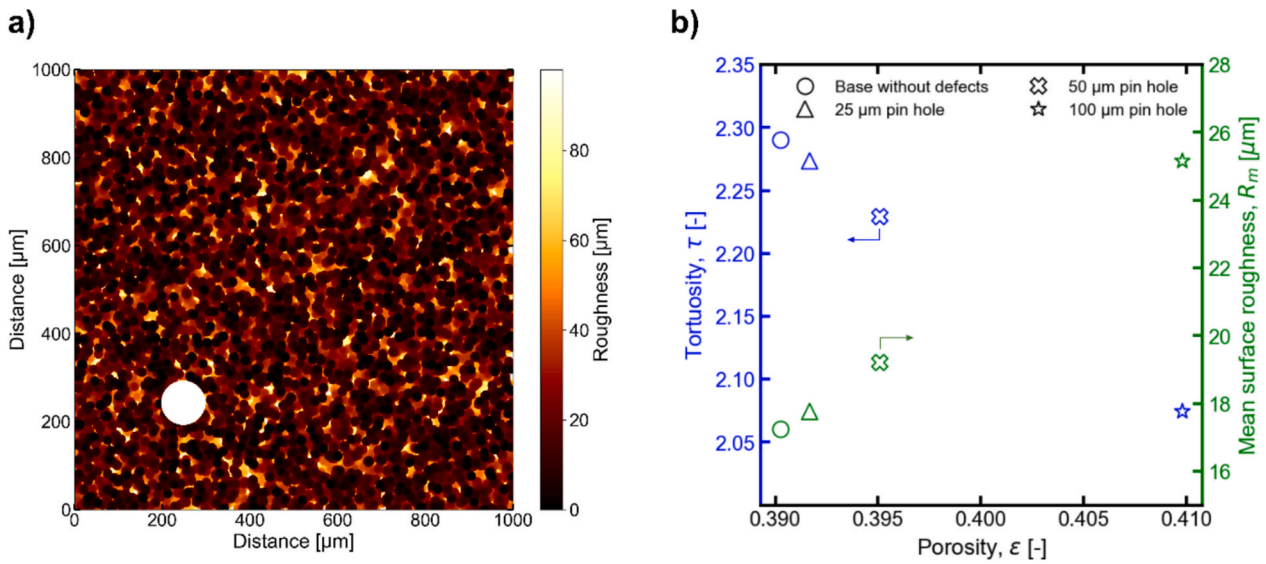

Fig. 4. (a) Surface roughness map for defect PTL with a 50 μm pinhole. (b) porosity versus tortuosity and surface roughness for defect PTLs with 25 μm, 50 μm, and 100 μm pinholes.

the baseline.

3.1.5. Cracks

Cracks have a minor impact on both pore size distribution and porosity profiles shown in the Supporting Information in Fig. S7. Cracks have minimal morphological impact because cracks are elongated void structures located on the outer surface of the defect PTL. The surface roughness map for the 20 μm crack is shown in Fig. 6a. Additionally, surface roughness maps for the 5 μm and 10 μm cracks are included in the supporting information in Fig. S3. Slightly higher roughness values occur at the crack location due to material removal in that area, resulting in a deeper depth. Average surface roughness values along with tortuosity results are quantified in Fig. 6b for each crack size to compare with the baseline. Results indicate that 5 μm, 10 μm, and 20 μm cracks have minimal effects on both tortuosity and the average surface roughness. Therefore, investigated cracks are not harmful for contact between CL and PTL because of their minimal effect on roughness, nor do they hinder single-phase transport due to their negligible impact on tortuosity.

3.1.6. Negative protrusion

Fig. S8 in the Supporting Information shows that negative protrusion sizes of 25 μm, 50 μm, and 100 μm have minimal impact on both pore size distribution and porosity profile. Because only a small portion of titanium was removed from a specific region of the PTL surface, negative protrusions had little effect on the morphological structure. Surface roughness map for negative protrusion size of 50 μm is shown in Fig. 7a, and mean roughness values for all mentioned sizes are quantified in Fig. 7b. Thus, the investigated negative protrusions will not negatively affect interfacial contact and catalyst utilization due to their minimal impact on roughness. They will also not compromise single-phase transport because of their limited influence on tortuosity. In fact, negative protrusions enhance transport properties in some cases, which will be discussed later in this article.

3.2. Impact of defects on transport properties

Examining how defects affect PTL's absolute and effective permeabilities is essential because these properties influence two-phase transport which inherently impact mass transport losses. Since water acts as the electrochemical reactant and oxygen as the product, improving permeability for both phases is crucial (i.e., higher gas permeability indicates better gas removal, and higher water permeability indicates better water transport). Single and effective permeability results were calculated using PNM in the through-plane z direction and in-plane x and y directions.

3.2.1. Detrimental transport consequences of defects: thickness variations and positive protrusions

Table 2 presents the directional absolute permeability results for defect PTL with 20%, 40%, and 60% thickness variations in the through-plane z direction and in-plane x and y directions. Since absolute permeability depends solely on the PTL structure, [47] its value varies with the added titanium material used to create the slanted surface due to changes in porosity and tortuosity in different directions. According to the Kozeny–Carman relation, absolute permeability increases with higher porosity and decreases with higher tortuosity. [48] In the through-plane z direction, absolute permeability values decrease slightly with greater thickness variation due to increased tortuosity caused by the more convoluted paths from the added titanium structure. In contrast, absolute permeability values increase significantly in the in-plane x,y directions due to the lower porosity of the void space in the slanted region. Since reactant delivery to the CL and product transport occur across the PTL thickness in the through-plane (z) direction, the decrease in single-phase permeability indicates that defect PTLs with thickness variations will experience higher mass transport overpotentials compared to baseline PTL.

During invasion percolation simulation, capillary forces control the percolation pathways within the hydrophilic titanium porous structure. [6] Fig. 8a ~ 8c show the directional single and effective permeability of oxygen and water, along with oxygen saturation across PTL thickness in the inset figures at 10%, 50%, and 95% oxygen inlet coverage for a defective PTL with 20%, 40%, and 60% thickness variation compared to the baseline, respectively. Regarding baseline PTL permeability results, two main trends are evident. Firstly, absolute permeability is always higher than effective permeability in all directions for all oxygen inlet coverages. This is normal because absolute permeability considers only one phase within the PTL structure, while effective permeability accounts for two phases, where one hinders the flow of the other. [49] Secondly, effective permeability decreases as oxygen coverage levels rise due to increased in-plane clustering of oxygen, which impedes water flow. Results in Fig. 8a ~ 8c show that all investigated thickness variation defects cause water effective permeability to drop to nearly zero in the through-plane direction. This occurs because of the void structure at

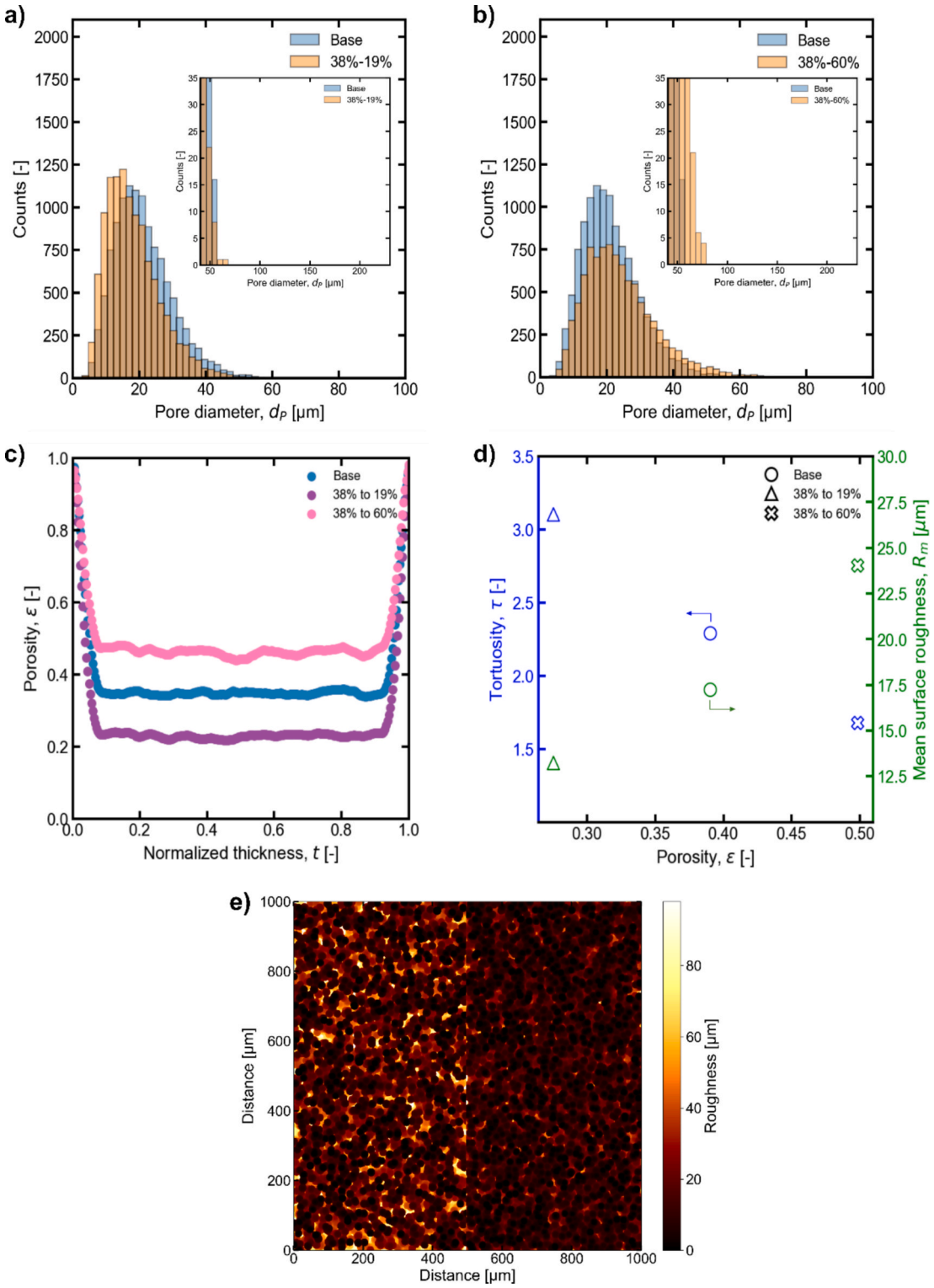

Fig. 5. Pore size distribution for defect PTLs with (a) 38%-19% and (b) 38%-60% porosity variations. (c) porosity profiles for defect PTLs with the same porosity variation cases. (d) porosity versus tortuosity and surface roughness for defect PTLs with the same porosity variation cases. (e) surface roughness map for defect PTLs with 38%-19% porosity variation.

the PTL/CL interface caused by the thickness variation defect. The void structure causes oxygen to accumulate inside it before proceeding to invade the pores of the first inclined layer of the defect PTL, thereby causing flooding of oxygen gas. The accumulated gas will prevent reactant water from passing across the PTL porous structure to reach reaction sites. This justification is supported by the analysis of saturation profiles shown in the inset figures. Regardless of the inlet oxygen coverage, oxygen saturation peaks at 100% within the first 10% of the PTL thickness in all thickness variation cases. Thickness variation defects thus have a catastrophic effect on transport because they prevent the delivery of water needed for the electrochemical reaction. All thickness-variation and positive-protrusion cases—across all defect sizes

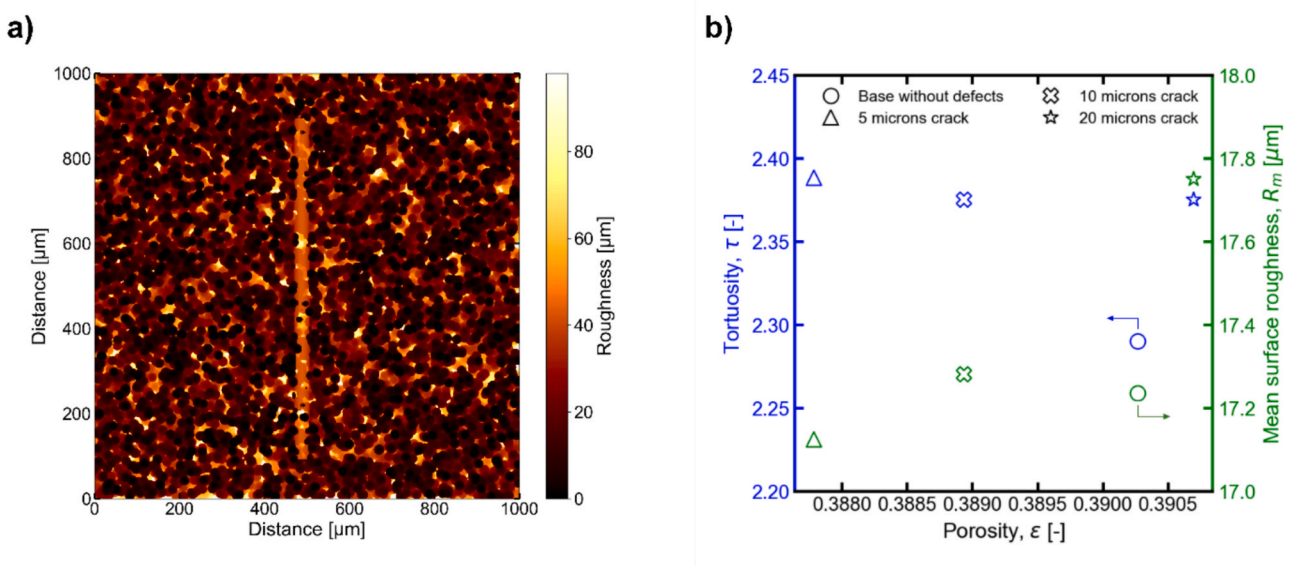

Fig. 6. (a) Surface roughness map of a defect PTL with a 20 μm crack. (b) porosity versus tortuosity and surface roughness for defect PTLs with crack sizes of 5 μm, 10 μm, and 20 μm.

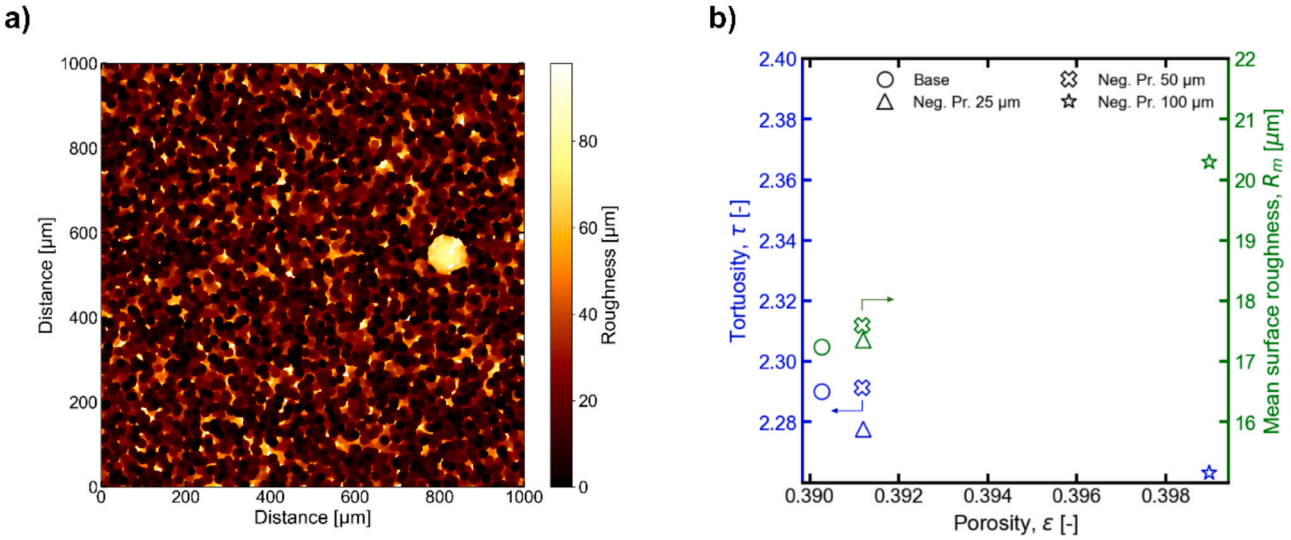

Fig. 7. (a) Surface roughness map of a defect PTL with a 50 μm negative protrusion. (b) Porosity versus tortuosity and surface roughness for defect PTLs with 25 μm, 50 μm, and 100 μm negative protrusions.

Table 2
Directional single-phase permeability of defect PTL with thickness variation.

PTL	Permeability, K_z [$\times 10^{-12}$ m^2]	Permeability, K_x [$\times 10^{-12}$ m^2]	Permeability, K_y [$\times 10^{-12}$ m^2]
Baseline	0.938	1.906	1.844
20% Thickness Variation	0.705	13.563	75.292
40% Thickness Variation	0.433	18.776	293.303
60% Thickness Variation	0.250	11.146	325.539

studied—create enlarged interfacial void regions that become rapidly saturated with oxygen during invasion, which directly corresponds to the near-zero water effective permeability observed in these cases. These results indicate that any defect that generates a large artificial void space at the PTL/CL interface (as opposed to the natural pore morphology of the baseline PTL) is inherently detrimental to reactant transport because it provides a preferential reservoir for oxygen accumulation. The artificial void space volumes caused by thickness variation and positive protrusion examined in this study are listed in the Supporting Information in Table S3. Regarding the in-plane x-y directions, water effective permeability also decreases significantly from the baseline value by approximately 80% to 90% at full oxygen coverage (high current density operation). All thickness variation defect results indicate that oxygen effective permeability rises sharply in the in-plane y direction, as the void space facilitates free oxygen flow in that direction without any porous structure impeding it. Oxygen effective permeability also increases in the in-plane x direction, but to a lesser degree than in the y direction, as part of the porous structure remains available in the void space region. Analyzing through-plane data is more critical because this is the primary direction in which oxygen generation and flow occur.

Directional single-phase permeability results for defect PTL with all positive protrusion cases are shown in Table 3. In the through-plane z

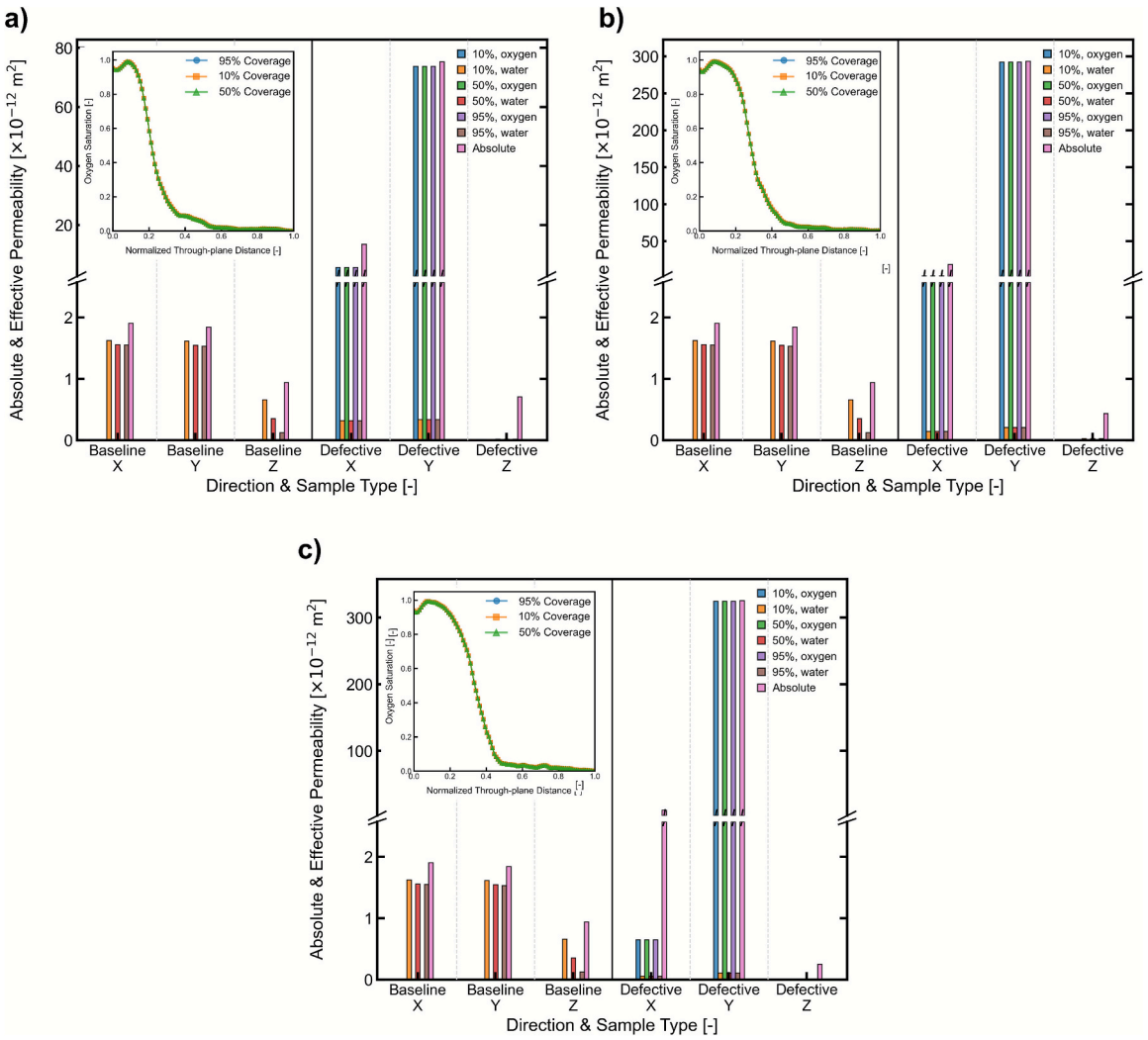

Fig. 8. Directional single and effective permeability of oxygen and water at 10%, 50%, and 95% oxygen inlet coverage for a defective PTL with (a) 20%, (b) 40%, and (c) 60% thickness variation compared to the baseline. The inset in each figure shows the oxygen saturation profile across the defect PTL thickness for each case at 10%, 50%, and 95% oxygen inlet coverage.

Table 3
Directional single-phase permeability of defect PTL with positive protrusions.

PTL	Permeability, K_z [$\times 10^{-12}$ m^2]	Permeability, K_x [$\times 10^{-12}$ m^2]	Permeability, K_y [$\times 10^{-12}$ m^2]
Baseline	0.938	1.906	1.844
25 μm Positive Protrusion	1.051	151.299	150.921
50 μm Positive Protrusion	1.143	607.177	707.558
100 μm Positive Protrusion	1.266	2696.456	2495.549

direction, single-phase permeability increases slightly with increasing protrusion size. This occurs as the volume of void space slightly increases, thereby enhancing total porosity, which subsequently increases permeability according to the Kozeny–Carman relation. In the in-plane x and y directions, single-phase permeability values increase significantly as the void space allows phase movement in both directions, resulting in a much lower pressure drop with increasing protrusion size when applying the Stokes flow algorithm.

The single and effective permeability of oxygen and water in all directions at 10%, 50%, and 95% inlet oxygen coverages for all positive protrusion cases investigated are shown in Fig. 9a ~ 9c. In the through-plane, z-direction, the water effective permeability approximately drops to zero for all positive protrusion cases and at all examined inlet oxygen coverages. This occurs because positive protrusion causes the formation of an entire layer of void space around it at the PTL/CL interface, causing delamination. Oxygen gas will then fill this void space before it starts to invade the first layer of the defect PTL, again causing flooding. This observation is also shown by the saturation profiles in Fig. 9a ~ 9c. Regardless of the inlet oxygen coverage, oxygen saturation peaks at 100% at 20%, 30%, and 40% of the defect PTL thickness for the 25 μm, 50 μm, and 100 μm positive protrusion cases, respectively. Similar to cases with thickness variation, oxygen build up in the delaminated region will block water pathways. As a result, the essential reactant water can no longer reach the electrochemical reaction sites.

In the in-plane x-y directions, the effective permeability of water decreases by approximately 80% across all protrusion cases and inlet oxygen coverage percentages. In contrast, oxygen's effective permeability rises sharply in both x and y directions because of the void space that allows oxygen to move freely.

3.2.2. *Beneficial transport Effects: Negative Protrusions, Cracks, and pinholes*

Fig. 10a shows single-phase permeability values in the through-plane

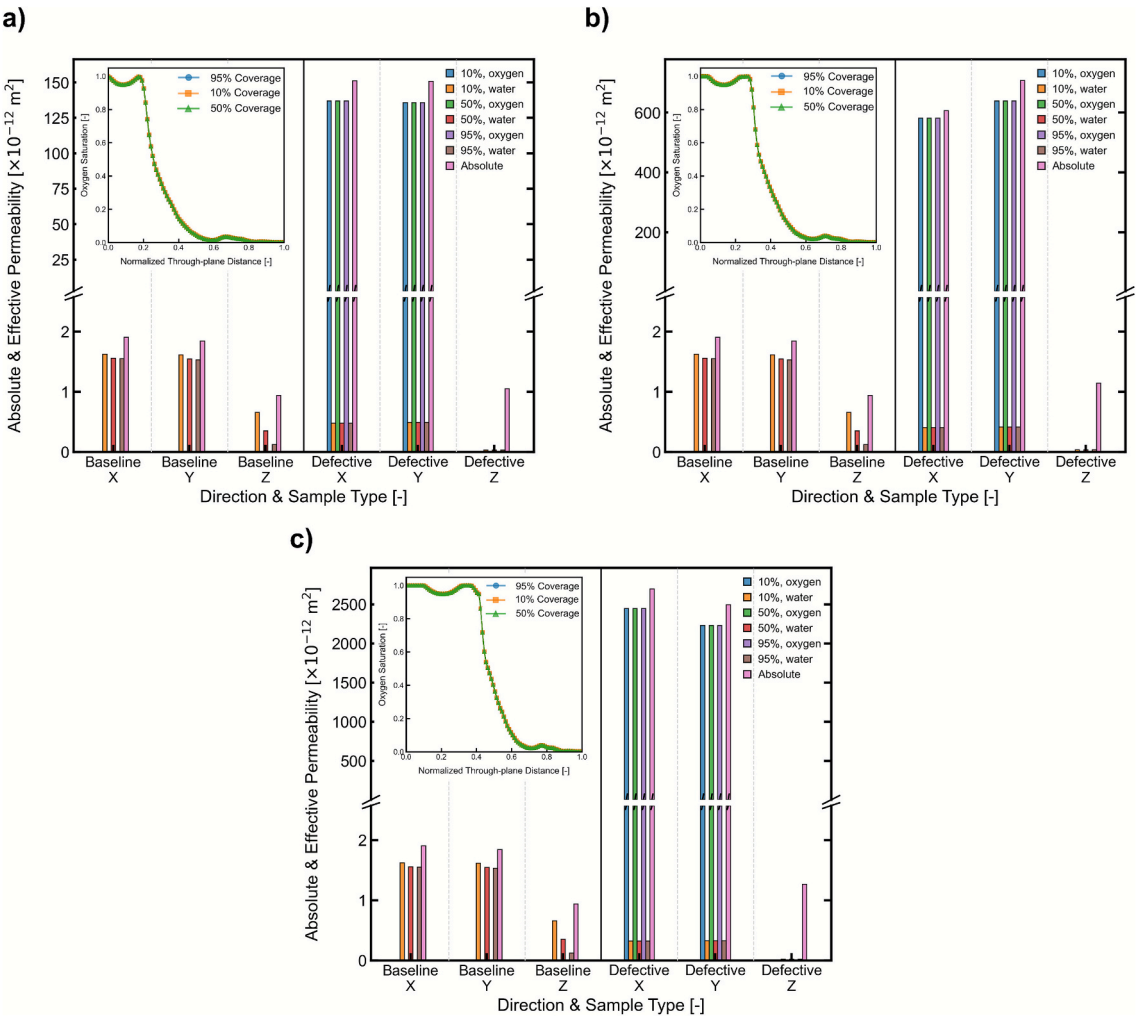

Fig. 9. Directional single and effective permeability of oxygen and water at 10%, 50%, and 95% oxygen inlet coverage for a defect PTL with (a) 25 μm, (b) 50 μm, and (c) 100 μm positive protrusions compared to the baseline. The inset in each figure shows the oxygen saturation profile across the defect PTL thickness for each case at 10%, 50%, and 95% oxygen inlet coverage.

z direction for defect PTLs with different crack, negative protrusion, and pinhole sizes. In addition, the numerical absolute permeability values in all directions are provided in Table S2 in the Supporting Information. Single-phase permeability is unaffected by cracks and negative protrusions since both of these defects are created on the outer surface of the PTL and have minimal impact on morphology. In contrast, absolute permeability increases significantly with larger pinholes compared to the baseline, as more titanium is removed from the bulk material, which greatly affects morphological properties like porosity and tortuosity. Higher porosity and lower tortuosity in defect PTLs with pinholes lead to a significant increase in absolute permeability, satisfying the Kozeny–Carman relation.

The effective water permeability in the through-plane z direction for defect PTLs with cracks, negative protrusions, and pinholes at oxygen inlet coverages of 95%, 50%, and 10% is shown in Fig. 10b ~ 10d, respectively. The 5 μm crack causes a small reduction in water effective permeability across all coverage scenarios, while cracks of 10 μm and 20 μm lead to a slight increase in permeability. This indicates that oxygen bubbles accumulation in larger crack sizes, regardless of oxygen inlet coverage or current density operation level, does not have a negative impact on water effective permeability. To support this conclusion, a prior experimental study by Tsushima et al. [50] similarly concludes that cracks in the MEA can facilitate liquid and gas transport in polymer-electrolyte fuel cells.

The defect PTL with a 5 μm negative protrusion size shows the highest water effective permeability in the through-plane direction compared to other negative protrusion sizes across all oxygen inlet coverage cases. Increasing the negative protrusion size to 10 μm and 20 μm results in reduced water permeability across all examined oxygen coverage scenarios. This is because oxygen accumulates at the protrusion site, blocking water pathways. However, at full oxygen coverage, all negative protrusion sizes exhibit higher effective permeability values compared to the baseline. This indicates that during high current density operation of PEM electrolyzers, defect PTLs of all sizes investigated in this study positively affect the water's effective permeability in the through-plane direction, with the 5 μm size expected to have the lowest mass transport overpotentials.

Enhanced effective water permeability in the through-plane direction across all pinhole sizes and inlet oxygen coverages is a promising indicator of reduced mass transport overpotential in PEM electrolyzers. Larger pinholes result in higher water effective permeability because oxygen can pass freely through the conduit, maintaining unobstructed water pathways. Furthermore, reducing the oxygen inlet coverage further enhances water effective permeability at lower current densities, as shown in Fig. 10b ~ 10d. Therefore, it can be argued that the pinhole defect actually acts as an engineered feature that assists mass transport, as previous demonstrated patterned-through pores. [19] It is important to take advantage of these defects that benefit the operation of PEM water electrolyzers.

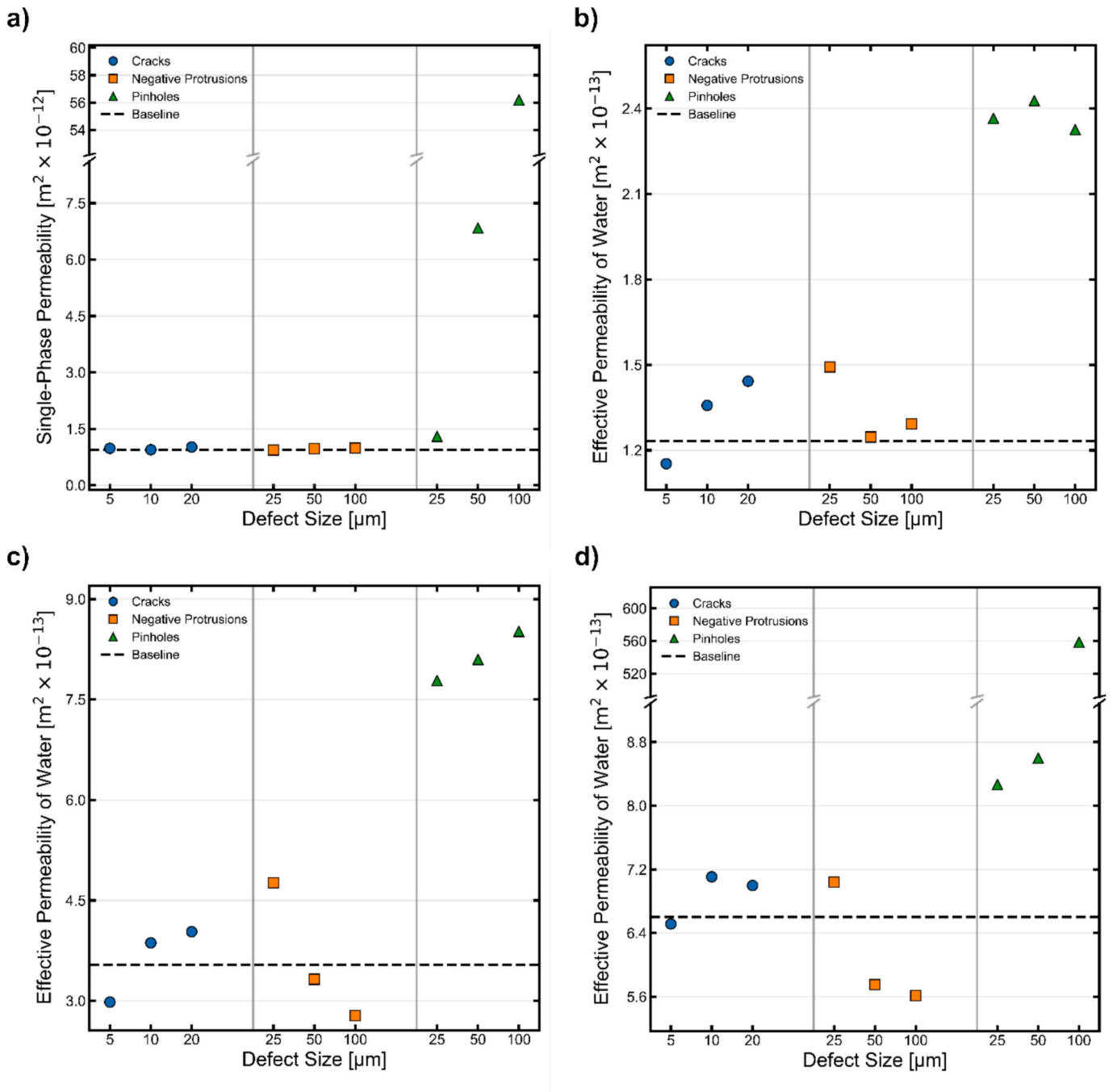

Fig. 10. (a) Absolute permeability in the through-plane z direction of defect PTLs with different cracks, negative protrusions, and pinhole sizes. Effective permeability of water in the through-plane z direction for defect PTLs with different crack, negative protrusion, and pinhole sizes at (b) 95%, (c) 50%, and (d) 10% oxygen inlet surface coverages.

3.2.3. *Porosity variation impact on transport*

Fig. 11a ~ 11b show the single and effective permeability at different oxygen inlet coverages of defect PTLs with porosity variations of 38%-19% and 38%-60%, respectively, along with the saturation profiles in the inset figures. In addition, the numerical absolute permeability values in all directions are provided in Table S2 in the Supporting Information. Single-phase permeability decreases as porosity drops from 38% to 19% and increases when porosity rises from 38% to 60% in all directions. This occurs because higher porosity provides more void volume for fluid (water/oxygen) to flow with less tortuosity, while lower porosity results in more convoluted paths. Saturation profiles shown in the inset figures show no oxygen blocking for either case; however, effective permeability values are significantly affected. Water effective permeability follows the same trend in all directions at all inlet oxygen coverages. This indicates that oxygen's impact on hindering water flow is more significant when porosity in the defect PTL is reduced and vice versa. Therefore, defect PTL with 38%–19% porosity variation is likely to exhibit higher mass transport overpotentials, whereas defect PTL with 38%–60% porosity variation may show lower mass transport overpotentials. However, it is noteworthy to understand that the gas percolation from these porosity variation PTLs always occur at the high porosity region, meaning that local gas saturation at the low porosity region remains low. Thus, in scenario of porosity variation defect, it can be speculated that there would be a preferential pathway for both

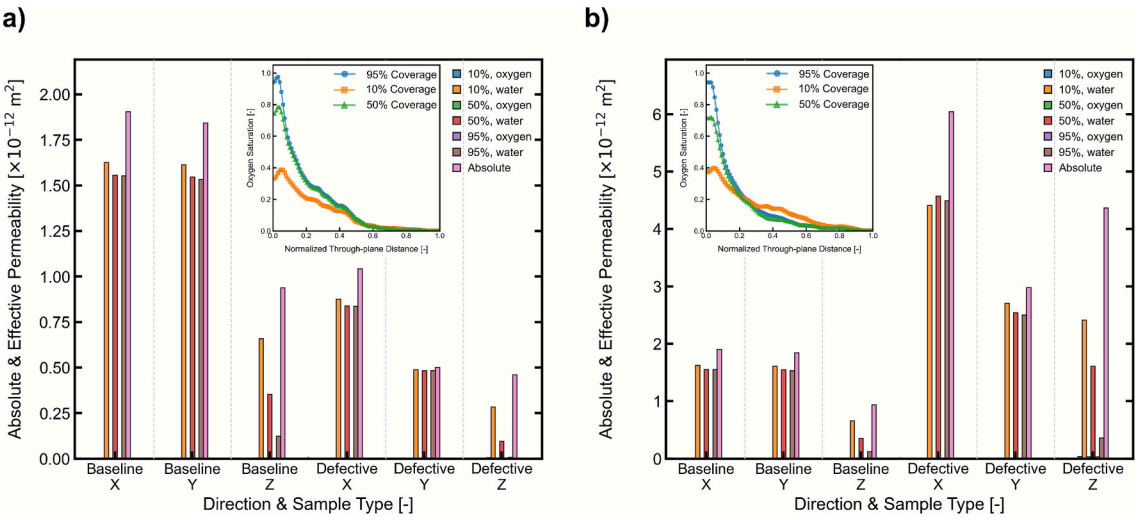

Fig. 11. Directional single and effective permeability of oxygen and water at 10%, 50%, and 95% oxygen inlet coverage for a defect PTL with (a) 38%-19% and (b) 38%-60% porosity. variation compared to the baseline. The inset in each figure shows the oxygen saturation profile across the defect PTL thickness for each case at 10%, 50%, and 95% oxygen inlet coverages.

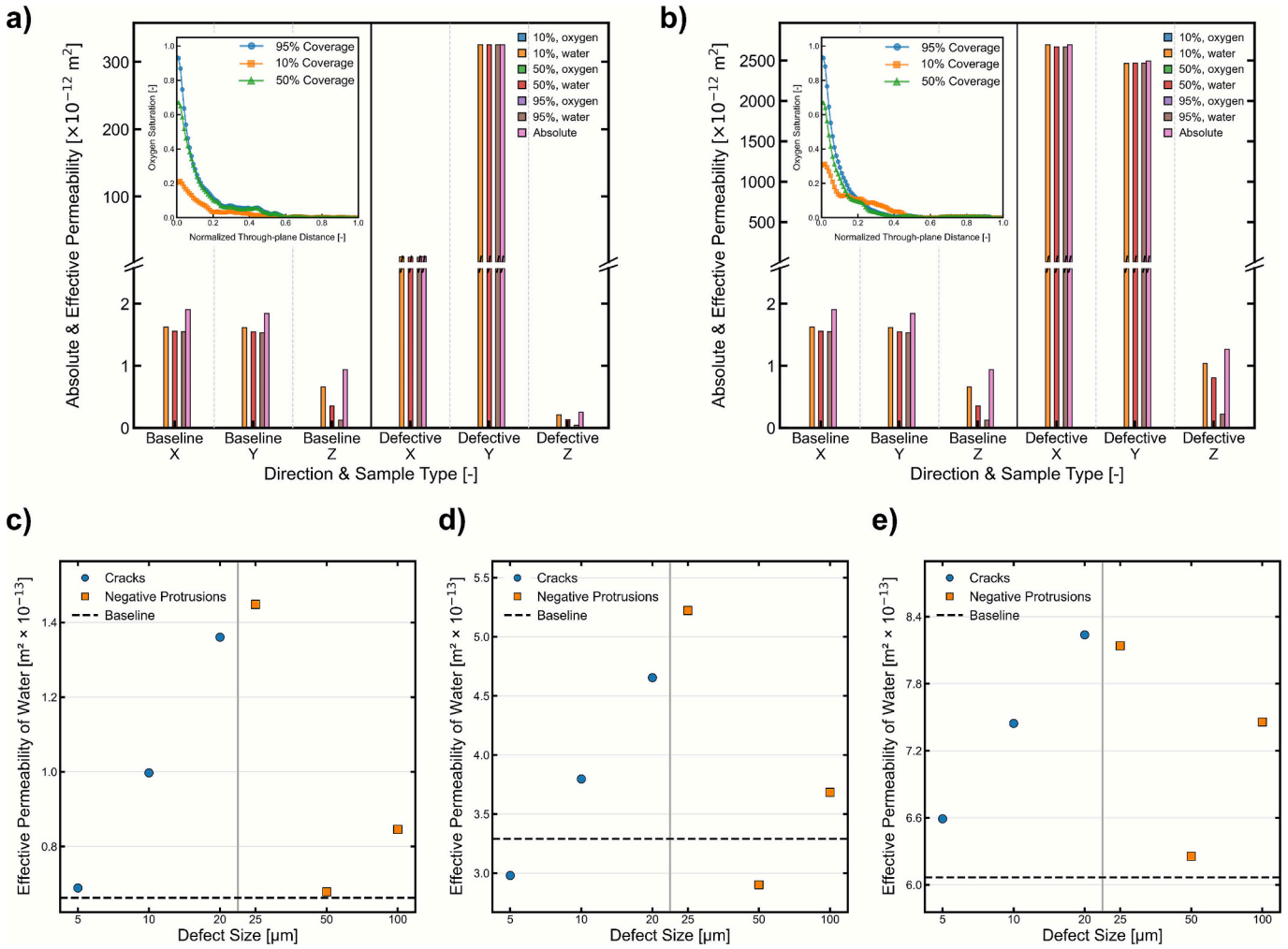

Fig. 12. Directional single and effective permeability of oxygen and water compared to the baseline at different oxygen inlet coverages for a defect PTL with (a) 60% thickness variation, (b) 100 μm positive protrusion. Effective permeability of water in the through-plane direction for different crack and negative protrusion sizes at (c) 95%, (d) 50%, and (e) 10% inlet oxygen coverage, where oxygen generation begins on the non-defect PTL side.

oxygen gas (high porosity region) and liquid water (low porosity region), which would in turn benefit the mass transport. The permeability and saturation trends predicted by our stochastic pore-network model are consistent with a recent experimental study on PEMWE porous transport layers. Lee et al. used custom Ti PTLs with patterned through-pores and in-operando neutron X-ray imaging to show that creating preferential through-plane pathways reduces gas saturation at the CL–PTL interface by ~ 43.5% and decreases mass-transport overpotentials by up to 76.7% at current densities up to 9 A cm^{-2}.

3.3. Effective remediation strategies for defect PTLs

All earlier results pertain to defects on the PTL surface adjacent to the CL. In section 3.2.1, we revealed that certain defects are detrimental to electrolyzer performance. For example, thickness variation and positive protrusion result in gas flooding at the interface between PTL and CL, thereby plummeting the effective permeability of liquid water. In this section, we show that by reorienting the PTL, performance of the electrolyzer will only improve due to the defect features. Specifically, as simple action of reversing the PTL direction will be an effective method for defect PTLs to attain optimal transport and better interfacial contact with the CL. Fig. 12a and 12b show the directional single and effective permeability of oxygen and water compared to the baseline at 10%, 50%, and 95% oxygen inlet coverage for the 60% thickness variation and 100 μm positive protrusion, respectively. Before reversing the defect PTL direction, the void space caused by the thickness variation and positive protrusion was located at the interface between CL and PTL. As previously discussed, this void leads to several serious problems, such as increased surface roughness, higher tortuosity, and most critically, creation of a delamination leading to accumulation of oxygen gases at the interface. This build up blocks water pathways and causes effective permeability in the through-plane direction to drop close to zero, preventing the necessary reactant water for electrochemical reactions from reaching the site.

After reorienting the defect PTL, the void space for both thickness variation and positive protrusion is now positioned beside the flow field. Fig. 12a ~ 12b show an improvement in water effective permeability in the through-plane z direction compared to the case before inverting PTL. This result can also be confirmed by analyzing saturation profiles across thickness at three different oxygen inlet coverages for PTL, with 60% thickness variation shown in the inset figures. Saturation profiles show that oxygen concentration declines smoothly in both cases, with no accumulation allowing water to reach reaction sites. In the in-plane x-y directions, there was a significant improvement in water effective permeability in both positive protrusion and thickness variation cases. This indicates that water distribution among the reaction sites will also improve due to better water effective permeability values in the in-plane directions. Similar trends were also observed for 20% and 40% thickness variations, as well as with the 25 μm and 50 μm positive protrusion directional absolute and effective permeability results shown in Fig. S9 in the Supporting Information. All these results suggest that PEM operation is now possible with a defect PTL that has thickness variations or positive protrusions after reversing the defect PTL direction.

Although a one-to-one experimental validation of effective permeability and oxygen saturation profile results for defect PTLs with delamination caused by thickness variation and positive protrusion was not conducted in this study, the main trends from our model are strongly supported by previous related experimental work. Lee et al. [51] quantified gas saturation across the PTL thickness using in operando synchrotron X-ray imaging and observed preferential gas accumulation and long-lived residual gas near the CL–PTL interface. This study supports our simulated oxygen saturation profiles, where thickness variations and positive protrusions create a much wider void space that worsens CL–PTL contact and leads to elevated gas saturation at the CL/PTL interface. In addition, Lee et al. [52] fabricated spatially graded sintered titanium PTLs by vacuum plasma spraying and examined them using in operando neutron imaging, electrochemical characterization, and pore-network modelling. They showed that orienting the graded PTL such that the lower-porosity region is adjacent to the catalyst layer and the higher-porosity region is adjacent to the flow field enables current densities up to 4.5 A cm^{-2} with a 29% reduction in cell potential, a 38% reduction in mass-transport overpotential, and a 50% reduction in PTL gas saturation, while enhancing the liquid–water permeability by approximately one order of magnitude compared with a non-graded reference. These results support our conclusion that defects in PTL morphology and the orientation of non-uniform or defected PTLs during assembly significantly affect oxygen saturation and effective water permeability.

Effective permeability of water for different negative protrusion and crack sizes at 95%, 50%, and 10% inlet oxygen coverage is shown in Fig. 12c ~ 12e, respectively. Reversing the defect PTL direction caused defect PTLs with cracks and negative protrusions—except for those with minimal fluctuations—to show increased water effective permeability across all examined defect sizes and oxygen inlet coverages. In fact, reorienting the PTL enables defects to be utilized as tailoed features that faciliate mass transport losses, which have been demonstrated experimentally. [53,54] Therefore, these types of defects can be used as an engineered feature that enhances mass transport while preserving the original interfacial contact of the PTL. Table 4 summarizes the qualitative trends of all parameters examined in this study.

4. Conclusions

In this study, we used stochastic and pore network modeling to examine the impact of defects in the PTL on their structural and transport properties. Defects of thickness variations and positive protrusions adversely affect structural properties, by creating undesired delamination between the PTL and CL, resulting higher surface roughness. They also negatively affect transport properties due to the delamination causing flooding of gas at the PTL/CL interface, driving water's effective permeability close to zero. When these defects are located near CL, reactant water cannot reach the electrochemical reaction sites, and operation is expected to halt. Some defects, including cracks, negative protrusions, and pinholes have minimal impact on surface roughness, but only improve both single and effective permeability, highlighting that these defects would be more beneficial than the regular PTLs. Cases of porosity variation primarily depend on morphological changes and adhere to the trade-off principles between porosity and surface roughness, but preferential pathways establish where gases will be evicted through high porosity region, and water would imbibe through the low porosity region. Finally, a proposed remediation strategy involves reorienting the PTL direction. This approach assists in mitigating the adverse effects of thickness variations and positive protrusions, while still maintaining transport benefits related to cracks and negative protrusions without impacting surface roughness. Implementing these strategies will greatly facilitate in identifying faulty PTLs and in

Table 4
Qualitative trends are indicated by arrows relative to the baseline. ↑↑ and ↓↓ indicate strong increase and strong decrease, respectively. ↑ and ↓ indicate an increase and a decrease, respectively. ↔ denotes minor impact. Symbols: R_s = surface roughness; τ = tortuosity; k_a = absolute permeability (through-plane); k_e = water effective permeability (through-plane).

Orientation	Defect Beside CL				Mitigated Orientation			
Defect type / Parameter	R_s	τ	K_a	K_e	R_s	τ	K_a	K_e
Thickness Variations	↑↑	↑↑	↓↓	↓↓	↔	↑↑	↓	↓
Positive Protrusions	↑↑	↑↑	↓↓	↓↓	↔	↑↑	↑	↑
38%-19% Porosity Variation	↓	↑	↓	↓	↓	↑	↓	↓
38%-60% Porosity Variation	↑	↓	↑	↑	↑	↓	↑	↑
Cracks	↔	↔	↑	↑	↔	↔	↑	↑
Pinholes	↑	↓	↑	↑	↑	↓	↑	↑
Negative Protrusions	↔	↔	↑	↑	↔	↔	↑	↑

minimizing the number of faulty PTLs.

CRediT authorship contribution statement

Abdullah Tayyem: Writing – review & editing, Writing – original draft, Visualization, Validation, Methodology, Investigation, Formal analysis, Data curation. **Victor Lefebvre:** Writing – review & editing, Writing – original draft, Visualization, Methodology, Investigation, Data curation. **Junghyuk Ko:** Writing – review & editing, Writing – original draft, Supervision. **Sung Ki Cho:** Writing – review & editing, Writing – original draft, Resources, Project administration, Investigation, Funding acquisition, Conceptualization. **Jong Hyun Jang:** Writing – review & editing, Writing – original draft, Resources, Project administration, Investigation, Funding acquisition, Conceptualization. **Jason Keonhag Lee:** Writing – review & editing, Writing – original draft, Validation, Supervision, Software, Resources, Project administration, Methodology, Investigation, Funding acquisition, Conceptualization.

Declaration of competing interest

The authors declare the following financial interests/personal relationships which may be considered as potential competing interests: Jason Keonhag Lee reports financial support was provided by Canada Research Chairs Program. Jason Keonhag Lee reports financial support was provided by Natural Sciences and Engineering Research Council of Canada. Jason Keonhag Lee reports financial support was provided by National Research Foundation of Korea. Jong Hyun Jang reports financial support was provided by National Research Foundation of Korea. Sung Ki Cho reports was provided by National Research Foundation of Korea. If there are other authors, they declare that they have no known competing financial interests or personal relationships that could have appeared to influence the work reported in this paper.

Acknowledgments

Financial support from the Canada Research Chairs Program (Canada Research Chair Tier II in Energy Systems Innovation) and the Natural Sciences and Engineering Research Council of Canada Discovery Grant (RGPIN-2025-03930) are gratefully acknowledged. Support from Accelerating Community Energy Transformation (ACET), through Canada First Research Excellence Fund is graciously acknowledged. National R&D Program through the National Research Foundation of Korea (NRF) funded by Ministry of Science and ICT (RS-2024-00409901) are also gratefully acknowledged.

Appendix A. Supplementary data

Supplementary data to this article can be found online at https://doi.org/10.1016/j.enconman.2025.120988

Data availability

Data will be made available on request.

References

[1] Bevacqua E, Schleussner C-F, Zscheischler J. A year above 1.5 °C signals that earth is most probably within the 20-year period that will reach the paris agreement limit. Nat Clim Chang 2025;15(3):262–5. https://doi.org/10.1038/s41558-025-02246-9.

[2] Rodríguez-Varela J, Alonso-Lemus IL, Savadogo O, Palaniswamy K. Overview: current trends in green electrochemical energy conversion and storage. J Mater Res 2021;36(20):4071–83. https://doi.org/10.1557/s43578-021-00417-w.

[3] Reznicek EP, Koleva MN, King J, Kotarbinski M, Grant E, Vijayshankar S, et al. Techno-economic analysis of low-carbon hydrogen production pathways for decarbonizing steel and ammonia production. Cell Rep Sustain 2025;2(4):100338. https://doi.org/10.1016/j.crsus.2025.100338.

[4] *Hydrogen Production: Overview and Issues for Congress*. https://www.congress.gov/crs-product/R48196 (accessed 2025-10-17).

[5] Wang CR, Stansberry JM, Mukundan R, Chang H-M-J, Kulkarni D, Park AM, et al. Proton exchange membrane (PEM) water electrolysis: cell-level considerations for gigawatt-scale deployment. Chem Rev 2025;125(3):1257–302. https://doi.org/10.1021/acs.chemrev.3c00904.

[6] Lee JK, Lee CH, Bazylak A. Pore network modelling to enhance liquid water transport through porous transport layers for polymer electrolyte membrane electrolyzers. J Power Sources 2019;437:226910. https://doi.org/10.1016/j.jpowsour.2019.226910.

[7] Xu C, Wang J, Wang J, Yang K, Li G, Gao W, et al. Structural optimization study on porous transport layers of sintered titanium for polymer electrolyte membrane electrolyzers. Appl Energy 2024;357:122541. https://doi.org/10.1016/j.apenergy.2023.122541.

[8] Doan TL, Lee HE, Shah SSH, Kim MJ, Kim CH, Cho HS, et al. A Review of the porous transport layer in polymer electrolyte membrane water electrolysis. Int J Energy Res 2021;45(10):14207–20. https://doi.org/10.1002/er.6739.

[9] Padgett E, Bender G, Haug A, Lewinski K, Sun F, Yu H, et al. Catalyst layer resistance and utilization in PEM electrolysis. J Electrochem Soc 2023;170. https://doi.org/10.1149/1945-7111/acee25.

[10] Mayyas, A.; Ruth, M.; Pivovar, B.; Bender, G.; Wipke, K. *Manufacturing Cost Analysis for Proton Exchange Membrane Water Electrolyzers*; NREL/TP–6A20-72740, 1557965; 2019; p NREL/TP–6A20-72740, 1557965. Doi: 10.2172/1557965.

[11] Qian M, Schaffer G, Bettles C. J Sinteri Titanium Alloys 2010:324–55. https://doi.org/10.1533/9781845699949.3.324.

[12] Lee JK, Bazylak A. Stochastic modelling for controlling the structure of sintered titanium powder-based porous transport layers for polymer electrolyte membrane electrolyzers. J Electrochem Soc 2019;166(13):F1000. https://doi.org/10.1149/2.0161913jes.

[13] Lee J, Bazylak A. Optimizing porous transport layer design parameters via stochastic pore network modelling: reactant transport and interfacial contact considerations. J Electrochem Soc 2020;167:013541. https://doi.org/10.1149/1945-7111/ab6557.

[14] Ito H, Maeda T, Nakano A, Hwang CM, Ishida M, Kato A, et al. Experimental study on porous current collectors of PEM electrolyzers. Int J Hydrog Energy 2012;37(9):7418–28. https://doi.org/10.1016/j.ijhydene.2012.01.095.

[15] Liu J, Takada M, Kerner F, Inoue Y, Schröder D. Reconstruction and modeling of porous transport layers based on x-ray computed tomography imaging. ACS Appl Energy Mater 2024;7(21):10092–101. https://doi.org/10.1021/acsaem.4c02193.

[16] Hierarchically Structured Porous Transport Layers for Polymer Electrolyte Water Electrolysis. No. 2019. Doi: 10.1002/aenm.201903216.

[17] Mo J, Kang Z, Yang G, Retterer ST, Cullen DA, Toops TJ, et al. Thin liquid/gas diffusion layers for high-efficiency hydrogen production from water splitting. Appl Energy 2016;177:817–22. https://doi.org/10.1016/j.apenergy.2016.05.154.

[18] Yang Y, Ouyang T, Tao D, Xu B, Li J, Huang J, et al. Improving mass transfer with surface patterning of the porous transport layer for PEM water electrolysis. Cell Rep Phys Sci 2025;6(2):102433. https://doi.org/10.1016/j.xcrp.2025.102433.

[19] Lee JK, Lee C, Fahy KF, Kim PJ, Krause K, LaManna JM, et al. Accelerating bubble detachment in porous transport layers with patterned through-pores. ACS Appl Energy Mater 2020;3(10):9676–84. https://doi.org/10.1021/acsaem.0c01239.

[20] Garkusha P, Geiger C, Bernauer C, Weiss T, Ernst M, Zaeh MF. Micro-perforation of the porous transport layer for proton exchange membrane water electrolyzer cells using ultrashort laser pulses. Procedia CIRP 2024;124:46–50. https://doi.org/10.1016/j.procir.2024.08.068.

[21] Biswal R, Syed AK, Zhang X. Assessment of the effect of isolated porosity defects on the fatigue performance of additive manufactured titanium alloy. Addit Manuf 2018;23:433–42. https://doi.org/10.1016/j.addma.2018.08.024.

[22] Jin MZ, Zhao TF, Chen CQ. The effects of micro-defects and crack on the mechanical properties of metal fiber sintered sheets. Int J Solids Struct 2014;51(10):1946–53. https://doi.org/10.1016/j.ijsolstr.2014.02.004.

[23] Liu YJ, Li SJ, Wang HL, Hou WT, Hao YL, Yang R, et al. Microstructure, defects and mechanical behavior of beta-type titanium porous structures manufactured by electron beam melting and selective laser melting. Acta Mater 2016;113:56–67. https://doi.org/10.1016/j.actamat.2016.04.029.

[24] *Designing Microporous Layers for Electrolyzers Using Stochastic Approach | JACS Au*. https://pubs.acs.org/doi/full/10.1021/jacsau.4c00199 (accessed 2025-12-02).

[25] Miličić T, Altaf H, Vorhauer-Huget N, Živković LA, Tsotsas E, Vidaković-Koch T. Modeling and analysis of mass transport losses of proton exchange membrane water electrolyzer. Processes 2022;10(11):2417. https://doi.org/10.3390/pr10112417.

[26] Lee JK, Lau GY, Sabharwal M, Weber AZ, Peng X, Tucker MC. Titanium porous-transport layers for PEM water electrolysis prepared by tape casting. J Power Sources 2023;559:232606. https://doi.org/10.1016/j.jpowsour.2022.232606.

[27] Zhao B, Lee C, Lee JK, Fahy KF, LaManna JM, Baltic E, et al. Superhydrophilic porous transport layer enhances efficiency of polymer electrolyte membrane electrolyzers. Cell Rep Phys Sci 2021;2(10):100580. https://doi.org/10.1016/j.xcrp.2021.100580.

[28] Alkhaldi S, Aziz M, Amrite A, Prasad AK. Parametric study of PEM water electrolyzer performance. J Appl Electrochem 2025;55(2):327–43. https://doi.org/10.1007/s10800-024-02187-9.

[29] Hackemüller FJ, Borgardt E, Panchenko O, Müller M, Bram M. Manufacturing of large-scale titanium-based porous transport layers for polymer electrolyte membrane electrolysis by tape casting. Adv Eng Mater 2019;21(6):1801201. https://doi.org/10.1002/adem.201801201.

[30] Zhu B, Duke M, Dumée LF, Merenda A, des Ligneris E, Kong L, Hodgson PD, Gray S. Short review on porous metal membranes—fabrication, commercial products, and applications. Membranes 2018;8(3):83. https://doi.org/10.3390/membranes8030083.

[31] Lee JK. Designing microporous layers for electrolyzers using stochastic approach. JACS Au 2024;4(6):2252–61. https://doi.org/10.1021/jacsau.4c00199.
[32] Kim PJ, Lee CH, Lee JK, Fahy KF, Bazylak A. In-plane transport in water electrolyzer porous transport layers with through pores. J Electrochem Soc 2020; 167(12):124522. https://doi.org/10.1149/1945-7111/abb173.
[33] Gostick JT. Versatile and efficient pore network extraction method using marker-based watershed segmentation. Phys Rev E 2017;96(2). https://doi.org/10.1103/PhysRevE.96.023307.
[34] Gostick J, Aghighi M, Hinebaugh J, Tranter T, Hoeh MA, Day H, et al. OpenPNM: a pore network modeling package. Comput Sci Eng 2016;18(4):60–74. https://doi.org/10.1109/MCSE.2016.49.
[35] Lee JK, Lee CH, Bazylak A. Pore network modelling to enhance liquid water transport through porous transport layers for polymer electrolyte membrane electrolyzers. J Power Sources 2019;437:226910. https://doi.org/10.1016/j.jpowsour.2019.226910.
[36] Altaf H, Vorhauer N, Tsotsas E, Vidaković-Koch T. Steady-state water drainage by oxygen in anodic porous transport layer of electrolyzers: a 2D pore network study. Processes 2020;8(3):362. https://doi.org/10.3390/pr8030362.
[37] Xu Y, Ye D, Zhang W, Wang Y, Li J, Zhang L, et al. Dual-scale pore network modeling of two-phase transport in anode porous transport layer and catalyst layer of proton exchange membrane electrolyzers. Energy Convers Manag 2024;322: 119089. https://doi.org/10.1016/j.enconman.2024.119089.
[38] Vorhauer N, Altaf H, Tsotsas E, Vidakovic-Koch T. Pore network simulation of gas-liquid distribution in porous transport layers. Processes 2019;7(9):558. https://doi.org/10.3390/pr7090558.
[39] Informatics, N. O. of D. and. *Oxygen*. https://webbook.nist.gov/cgi/cbook.cgi?ID=7782-44-7 (accessed 2025-10-22).
[40] Arbabi F, Montazeri H, Abouatallah R, Wang R, Bazylak A. Three-dimensional computational fluid dynamics modelling of oxygen bubble transport in polymer electrolyte membrane electrolyzer porous transport layers. J Electrochem Soc 2016;163:F3062–9. https://doi.org/10.1149/2.0091611jes.
[41] Lee JK, Lee C, Fahy KF, Zhao B, LaManna JM, Baltic E, et al. Critical current density as a performance indicator for gas-evolving electrochemical devices. Cell Rep Phys Sci 2020;1(8).
[42] Bryant S. Prediction of relative permeability in simple porous media. Phys Rev A 1992;46(4):2004–11. https://doi.org/10.1103/PhysRevA.46.2004.
[43] Heinemann, Z. E. Fluid Flow In Porous Media.
[44] Cooper SJ, Bertei A, Shearing PR, Kilner JA, Brandon NP. TauFactor: an open-source application for calculating tortuosity factors from tomographic data. SoftwareX 2016;5:203–10. https://doi.org/10.1016/j.softx.2016.09.002.
[45] Liu C, Padgett E, Arregui-Mena JD, Shepherd M, Ware S, Pylypenko S, et al. Performance improvement of proton exchange membrane water electrolysis by surface modification of porous transport layers. J Power Sources 2025;652: 237624. https://doi.org/10.1016/j.jpowsour.2025.237624.
[46] Peng X, Satjaritanun P, Taie Z, Wiles L, Keane A, Capuano C, et al. Insights into interfacial and bulk transport phenomena affecting proton exchange membrane water electrolyzer performance at ultra-low iridium loadings. Adv Sci 2021;8(21): 2102950. https://doi.org/10.1002/advs.202102950.
[47] Stiber S, Balzer H, Wierhake A, Wirkert FJ, Roth J, Rost U, et al. Porous transport layers for proton exchange membrane electrolysis under extreme conditions of current density, temperature, and pressure. Adv Energy Mater 2021;11(33): 2100630. https://doi.org/10.1002/aenm.202100630.
[48] Maier M, Smith K, Dodwell J, Hinds G, Shearing PR, Brett DJL. Mass transport in PEM water electrolysers: a review. Int J Hydrog Energy 2022;47(1):30–56. https://doi.org/10.1016/j.ijhydene.2021.10.013.
[49] Heinemann Z. *Fundamental properties of porous media: permeability and capillary pressure*. In: *Fluid Flow in Porous Media*. Montanuniversität Leoben: Leoben, Austria; 2013. p. 1–53.
[50] Tsushima S, Hirai S. An overview of cracks and interfacial voids in membrane electrode assemblies in polymer electrolyte fuel cells. J Therm Sci Technol 2015;10 (1). https://doi.org/10.1299/jtst.2015jtst0002. JTST0002–JTST0002.
[51] Lee CH, Lee JK, Zhao B, Fahy KF, Bazylak A. Transient gas distribution in porous transport layers of polymer electrolyte membrane electrolyzers. J Electrochem Soc 2020;167(2):024508. https://doi.org/10.1149/1945-7111/ab68c8.
[52] Lee JK, Lee C, Fahy KF, Kim PJ, LaManna JM, Baltic E, et al. Spatially graded porous transport layers for gas evolving electrochemical energy conversion: high performance polymer electrolyte membrane electrolyzers. Energy Convers Manag 2020;226:113545. https://doi.org/10.1016/j.enconman.2020.113545.
[53] Tugirumubano A, Seip T, Zhu L, Ham CT, Farsi A, Bazylak A. Integrated-Channel porous transport layers reduce ohmic and mass transport losses in polymer electrolyte membrane electrolyzers. Adv Funct Mater 2025;35(1):2410262. https://doi.org/10.1002/adfm.202410262.
[54] Lee JK, Schuler T, Bender G, Sabharwal M, Peng X, Weber AZ, et al. Interfacial engineering via laser ablation for high-performing PEM water electrolysis. Appl Energy 2023;336:120853. https://doi.org/10.1016/j.apenergy.2023.120853.